European Journal of Mechanics / A Solids 115 (2026) 105826

Contents lists available at ScienceDirect

European Journal of Mechanics / A Solids

journal homepage: www.elsevier.com/locate/ejmsol

Full Length Article

Mitigation of vertical vibrations in coupled meta-rods through internal interactions and boundary constraint

Haoran Lu [a], Jacopo M. De Ponti [b], Raffaele Ardito [b], Li Xiao [a], Yuanqiang Cai [a], Zhigang Cao [a,*]

[a] College of Civil Engineering and Architecture, Zhejiang University, Hangzhou, China
[b] Department of Civil and Environmental Engineering, Politecnico di Milano, Milano, Italy

ARTICLE INFO

Keywords:
Locally resonant metamaterial
Coupled elastic bars
Low-frequency
Vibration control
External constraints
Negative stiffness

ABSTRACT

Environmental vibrations caused by seismic waves and traffic loads pose increasing risks in urban areas due to their low attenuation and structural impact. To mitigate the in-plane bulk waves and vertical Raleigh wave component generated by ambient vibrations, we proposed a coupled meta-rod assembled from a local resonance (LR) bar and a negative-stiffness (NS) system. This meta-rod is designed in two forms to redistribute the wave energy, where the NS system is introduced as a boundary constraint. We develop analytical models based on the Bloch conditions and the transfer matrix method to solve and investigate dispersion relationship and transmission abilities. Complementarily, finite elements (FE) models are also established to validate the analytical results and further visualise the interaction between the LR bar and NS system during longitudinal wave propagation. The results indicate that most of long-wavelength waves propagate through the low-stiffness medium within the coupled system. As wave energy is redistributed across frequency, an additional attenuation region emerges beyond the LR bandgap due to the maximum in-phase motion between the LR bar and NS system. This internal interaction gradually dominates the attenuation mechanism as the LR bandgap shifts toward lower frequencies under boundary constraints, providing more effective suppression before the resonance frequency. This study offers a promising strategy for the design of efficient vertical vibration mitigation solutions.

1. Introduction

Environmental vibrations induced by traffic or seismic activities are persistent and recurrent, propagating outward through the soil in the form of elastic waves. These vibrations are composed of a broad range of low-frequency and long-wavelength components, that are correlated to low attenuation rates. They can significantly disrupt sensitive equipment (Clouteau et al., 2001; Kuo et al., 2019; Yu et al., 2020) and adversely impact on the life quality of residents in affected areas (Griefahn et al., 2006). The traffic-induced vibrations generally occur within the frequency range of 1–80 Hz (Thompson et al., 2019), while the main seismic wave energy typically lies within a narrower band of 1–10 Hz (Kanellopoulos et al., 2022). The widespread nature of these dynamic characteristics poses a challenge in designing protective measures for shielding against ambient vibrations.

To attenuate in-plane polarised waves (bulk and surface) generated by environmental vibrations, many efforts have been made to develop wave screening structures and seismic protection systems. The most common measures include using trenches and pile barriers along the vibration transmission path (Barkan, 1962; Woods, 1968; Woods et al., 1974; Segol et al., 1978; Gao et al., 2006; Cao and Cai, 2013; Brûlé et al., 2014; Thompson et al., 2016; Ramaswamy et al., 2023), or installing energy-damping devices within the protected structures (Setareh, 2001; Ali and Ramaswamy, 2009; Tuan and Shang, 2014; Chang et al., 2018; Christopoulos and Filiatrault, 2022; Jiang et al., 2024). The former isolation measures essentially work depending on the mechanical impedance ratio between the surrounding soil and inclusions. By embedding materials with differential impedance into the soil, the high-frequency waves with short wavelengths will be desirably isolated or reflected during their propagation. However, the impedance mismatch mechanism is difficult to implement effectively for the relatively low-frequency range due to the requirement for large or even impractical geometric dimensions. For this reason, damping devices become one of the most widely used methods by shifting the structural resonances away from the most energetic frequencies of seismic spectra (Palermo et al., 2016). A more evident control effect in the low frequency can be achieved by increasing the mass size of these damping devices (Feng and Mita, 1995; Fang et al., 2021, 2024). However, this

* Corresponding author.
E-mail address: caozhigang2011@zju.edu.cn (Z. Cao).

https://doi.org/10.1016/j.euromechsol.2025.105826
Received 10 June 2025; Received in revised form 30 July 2025; Accepted 4 August 2025
Available online 5 August 2025

increase in mass size implies larger stresses and a greater amount of material, which may be impractical for most applications.

In the context of elastodynamics, the advent of mechanical metamaterials has inspired diverse approaches towards controlling the propagation characteristics of elastic waves. Among diverse mechanisms arising from the special ordering of internal space, the local resonance (LR) mechanism shows a remarkable ability to manipulate and attenuate elastic waves at sub-wavelength scales (Sugino et al., 2018; Zheng et al., 2024; Han et al., 2025; Wang et al., 2025), primarily due to the hybridisation of internal resonant modes (Liu et al., 2000; Colquitt et al., 2017). Recently, inspired by the stiffness counterbalance phenomenon, researchers have incorporated the concept of negative stiffness (NS) into LR mechanical metamaterials, proving a viable approach to lowering the resonant frequency without the requirement of increased mass (Carrella et al., 2012; Huang et al., 2014; Song et al., 2019; Tan et al., 2022, 2024a; Demir and Yilmaz, 2022; Jiao et al., 2023; Zhou et al., 2024). The fundamental concept of this mechanism involves utilising geometric and force nonlinearities to effectively reduce the stiffness of the isolator. To bring this to fruition, the unstable phenomena have been skilfully utilised through the use of post-buckling beams, perforated plates, shell structures, multiple magnet systems, origami, compressed springs, and so on (Dalela et al., 2022; Tan et al., 2024b). Notably, Zhou et al. (Zhou et al., 2017; Cai et al., 2020) presented a quasi-zero stiffness metamaterial composed of folding beams or oblique compression springs, enabling a lower bandgap while ensuring load-bearing performance. Building on this, Wang et al. (2021) introduced a novel negative-stiffness mechanism (NSM) into the resonator for facilitating the neutralisation of translational and torsional stiffness. By adjusting the parameters of the NSM, this work offers a flexible way to tune the LR bandgap within a large frequency range. When the positive- and negative-stiffness materials exhibit nearly equal absolute stiffness, the equivalent stiffness of the whole system tends toward infinity, which represents extremely high practical stiffness. Lakes et al. (Lakes, 2001; Lakes et al., 2001) embedded NS materials as inclusions in a positive stiffness matrix, thus preserving a sufficiently stiff matrix and thereby ensuring structural stability. Kochmann and Milton (2014) established mathematical limits on the modulus of elasticity for composites incorporating NS components to ensure structural stability. Mei et al. (2023) also suggested that NS units can maintain stability under appropriate constraints.

In civil engineering, elastically supported foundations are usually modelled as a series of closely spaced, mutually independent, and linear elastic springs, offering vertical or horizontal resistance proportional to the deflection of structures (Makris and Gazetas, 1992; Cabello et al., 2016; Rodrigues et al., 2018; Zemskov and Van Hao, 2025). Inspired by these external constraints, Xu et al. (2023) and Lin et al. (2021) investigate the quasi-static bandgap characteristics of meta-chains composed of a series of grounded NS springs, which evidently provide a more effective attenuation coefficient at lower frequencies. Similarly, Xiao et al. (2024) proposed a new configuration of periodically supported pipes equipped with NS resonators, achieving a significantly broader LR bandgap than traditional resonators under the same mass. Moreover, researchers have found that external boundary constraints, such as bedrock layers (Achaoui et al., 2017; Maheshwari and Rajagopal, 2022; Wang et al., 2023) or rigid external supporting (Lu et al., 2024), also bring more structural stability and wave attenuation within the target abatement spectra. Lu et al. (2024) developed an improved formulation to explore the mechanical behaviour and wave attenuation performance of meta-rod, revealing how external boundary constraints remarkably improve its dynamic performance. Although rigid external constraints represent a strong assumption in realistic scenarios involving complex environmental vibrations, the aforementioned studies have enabled the practical integration of existing constraints with NS elements in civil engineering applications. Following this principle, researchers have recently introduced artificial elastic or rigid constraints oriented parallel to the host structure. Specifically, Chen et al. (Chen and Elbanna, 2017) introduced a new mechanism for generating bandgaps with substantial attenuation by coupling continuous elastic rods with constraints and springs. Liu et al. (2016) fixed steel bars around the positive stiffness matrix to activate the negative effective mass of the whole structure in the low-frequency range. Subsequently, Nhi H. Vo et al., 2021, 2022 applied this concept to a meta-truss composed of two thin skins rigidly connected to the meta-lattice trusses. These innovations inspired the idea of developing a coupled meta-rod coupling with external artificial constraints to effectively mitigate the environmental vibrations in different spectra.

Hence, this study aims to propose an effective coupled meta-rod based on the negative stiffness mechanism to mitigate the in-plane polarised bulk waves and vertical Rayleigh waves components generated by ambient vibrations. By employing an outer pipe surrounding the inner elastic LR rod, the structure is designed to redistribute the wave energy through the connected NS system while maintaining the stability of the system. We developed an improved formulation for the coupled LR on both surface and interior of the foundation to solve their dispersion relation properties and wave attenuation behaviour. Then, how the internal interaction and boundary constraints of the proposed coupled meta-rod govern their attenuation ability in different ranges is investigated. Complemented by wave field analysis, the mutual motion in influencing the propagation characteristics is further confirmed in two application scenarios.

The remainder of this paper is as follows: we first introduce the configuration and physical model of coupled meta-rod for vertical vibration mitigation in Section 2. Section 3 develops the analytical framework based on the Bloch condition and transfer matrix method (TMM). Besides, in Section 4, a numerical method is also established to investigate the interaction within the proposed structure as a complement and comparison to the analytical results. In Section 5, we discuss the application of the proposed structure as meta-column and meta-pile in two vibration scenarios, revealing the attenuation mechanisms induced by the internal mutual motion and boundary constraints effect. The practical issues and options of the proposed structure are discussed in Section 6. Finally, conclusions and future outlooks are summarised in Section 7.

2. Coupled meta-rod configurations for vertical vibration mitigation

Environmental vibrations-induced elastic waves include bulk waves (P-waves and S-waves) propagating downward or upwards within the ground, and surface waves (Rayleigh waves) travelling along the ground surface. Among these, vertical components, which may induce significant structural displacements, have attracted considerable attention, especially in scenarios involving precision instruments (DeBra, 1992; Zhang et al., 2024). Therefore, this study primarily focuses on the vertical Raleigh wave component generated by traffic loads and bulk waves arising from seismic actions. To shield target equipment or buildings from these vertical vibrations, we propose an LR rod integrated with an NS system, which is installed both on surface and interior of the foundation (see Fig. 1). By adjusting the geometric parameter, this coupled meta-rod is designed in forms of meta-column and meta-pile to redistribute the wave energy under complex environmental vibration.

The unit cell of coupled meta-rod consists of three components: elastic (inner) rod, resonator, and NS system, as shown in Fig. 1. The resonator is attached to the elastic rod, typically inducing an LR bandgap at sub-wavelength scales. The NS system is implemented by applying pre-compression to springs connected to an outer pipe. When the vertical Rayleigh wave component or bulk waves are incident on the coupled meta-rod, the inner resonator, comprising a metal ring and a rubber ring, oscillates primarily in the vertical direction. A strong wave–structure interaction is excited when the frequency of the incident wave is close to the local resonance (LR) frequency of the inner resonator, leading to the formation of a LR bandgap. The starting frequency

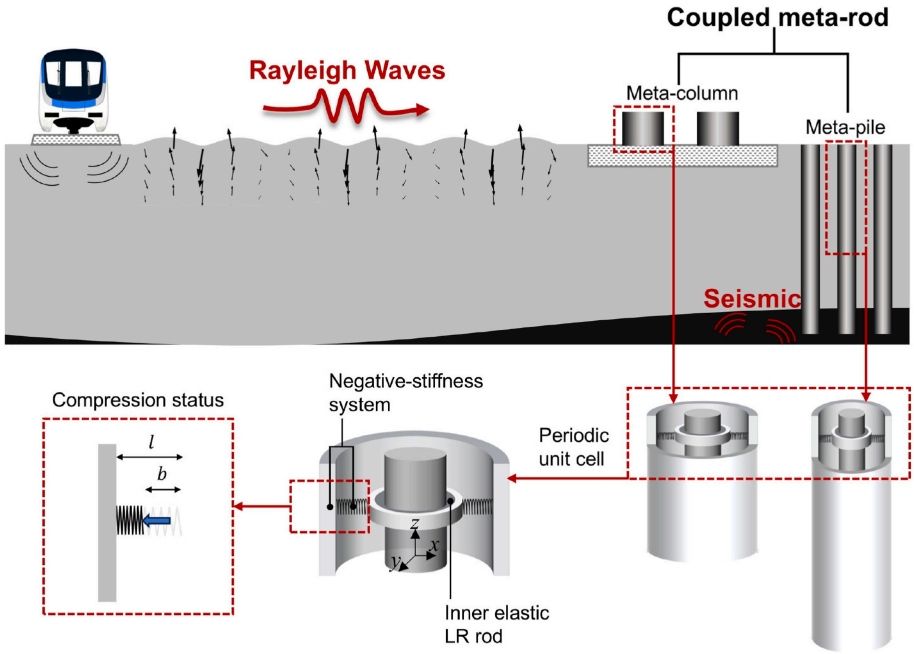

Fig. 1. Schematic of the proposed coupled meta-rods for mitigating vertical vibrations induced by traffic loads and seismic.

of this LR bandgap can be lowered through coupling with NS system. The outer pipe, acting as an external artificially induced constraint, influences the dynamic behaviour of whole structure by modulating the internal thrust force generated within the NS system. Adjusting its stiffness enables control over the position and width of bandgap. Thus, we can simultaneously leverage both boundary constraints effect and internal interaction to mitigate vertical vibrations generated by traffic and seismic excitations, especially in a lower frequency range.

3. Analytical model

In this section, the analytical models of the coupled meta-rod are developed to investigate dispersion relation properties and transmissibility. We start with the presentation of a physical model, detailing the structural components and their forced status under the vertical vibrations. Then the interaction between outer pipe and inner rod is captured by representing it as a series of interacting forces. By applying the continuity condition of stress, the motion equations for longitudinal wave propagation in two components are coupled and solved. The analytical exploration then proceeds to derive the dispersion relation based on the Bloch condition and boundary continuity condition. Moreover, the transmissibility is also derived by using TMM to declare the mutual motion within structures.

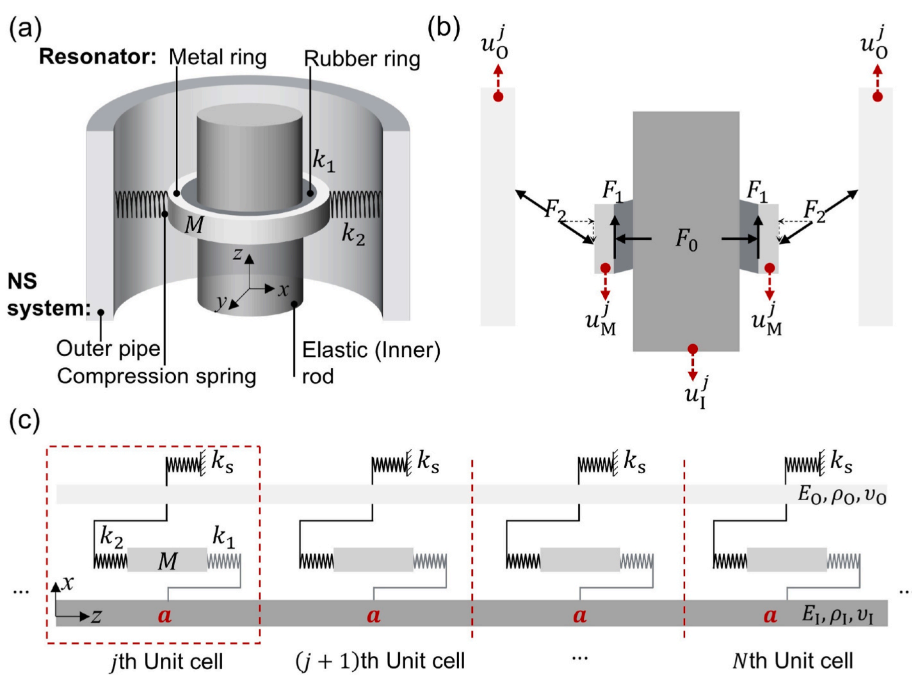

Fig. 2. The analytical model of coupled meta-rods. (a) Structural components of the unit; (b) Static analysis under the action of vertical vibrations; (c) Computational model for dispersion relation and transmissibility analysis.

3.1. Dispersion relation

Generally, vibration responses with strains less than or equal to 10^{-5} orders of magnitude are regarded as elastic responses. In the context of this assumption, each component including inner rod, rubber ring, metal ring, and outer pipe (see Fig. 2(a)) is modelled as a homogeneous and linear elastic material with Young's modulus (E), density (ρ), and Poisson's ratio (υ). As shown in Fig. 2(b), the movement of the jth inner rod ($u_{\mathrm{I}}^{j}(z)$) under the vertical excitation results in the dynamic response within the resonator ($u_{\mathrm{M}}^{j}(z)$). A displacement difference is induced between the resonator and the outer pipe ($u_{\mathrm{O}}^{j}(z)$), leading to a release of the compression spring. Assuming that the force within the resonator, supplied by the rubber ring, can be decomposed into two independent parts in both horizontal (F_0) and vertical directions (F_1), then the force released by compression spring (F_2) can be balanced or partially counteracted by these two forces. More details about the NSM and its effect on mechanical properties can be found in the work of Lu et al. (2024).

This section aims at performing the eigenvalue analysis of infinite periodic units based on the computational model illustrated in Fig. 2(c). The resonator is simplified as a positive-stiffness (k_1) spring and a mass block (M) connected to a negative-stiffness (k_2) spring. Moreover, as stated in Section 2, the second application scenario for the proposed coupled meta-rods is installed within the foundation. To investigate more boundary constraints effects, a series of mutually independent and linear elastic vertical springs (k_s) are adopted against the direction of motion to represent the surrounding soil effect under the small strain assumption (Yang and Hung, 1997). It's necessary to note that these springs are set to zero in the first application scenario where soil action is absent. Under the above assumptions and simplifications, the governing equation of both propagation media with longitudinal motion is

$$\frac{\partial^2 u_{\mathrm{I}}(z,t)}{\partial t^2} = c_{\mathrm{I}}^2 \frac{\partial^2 u_{\mathrm{I}}(z,t)}{\partial z^2}, \tag{1.a}$$

$$\frac{\partial^2 u_{\mathrm{O}}(z,t)}{\partial t^2} = c_{\mathrm{O}}^2 \frac{\partial^2 u_{\mathrm{O}}(z,t)}{\partial z^2}, \tag{1.b}$$

where $u_{\mathrm{I}}(z,t), u_{\mathrm{O}}(z,t)$ denote the longitudinal displacement of inner rod and outer pipe, respectively; $c_{\mathrm{I}}, c_{\mathrm{O}}$ is the longitudinal wave speed of two propagation media with different materials. The longitudinal wave speed generally can be calculated by $c = \sqrt{E/\rho}$. Considering a steady state solution with the form $u(z,t) = U(z)e^{-\mathrm{i}\omega t}$, the displacement in inner rod can be given by:

$$\begin{cases} U_{\mathrm{I,L}} = A_1 \cos\left(\dfrac{\omega}{c_{\mathrm{I}}} z\right) + A_2 \sin\left(\dfrac{\omega}{c_{\mathrm{I}}} z\right) \\ U_{\mathrm{I,U}} = A_3 \cos\left(\dfrac{\omega}{c_{\mathrm{I}}} z\right) + A_4 \sin\left(\dfrac{\omega}{c_{\mathrm{I}}} z\right) \end{cases}. \tag{2.a}$$

Similar to the outer pipe, the displacement can be expressed by:

$$\begin{cases} U_{\mathrm{O,L}} = A_5 \cos\left(\dfrac{\omega}{c_{\mathrm{O}}} z\right) + A_6 \sin\left(\dfrac{\omega}{c_{\mathrm{O}}} z\right) \\ U_{\mathrm{O,U}} = A_7 \cos\left(\dfrac{\omega}{c_{\mathrm{O}}} z\right) + A_8 \sin\left(\dfrac{\omega}{c_{\mathrm{O}}} z\right) \end{cases}, \tag{2.b}$$

where $U_{\mathrm{I,L}}, U_{\mathrm{I,U}}, U_{\mathrm{O,L}}, U_{\mathrm{O,U}}$ denote the mode shape of lower and upper half of inner rod, and outer pipe respectively; z is axis coordinates within $[0, a]$; a is known as the lattice constant, which denotes the length of a unit cell. There are eight unknown coefficients for these four mode shapes, denoted as $A_1, A_2 \ldots A_8$. According to the Bloch condition $U(0) = U(a)e^{-\mathrm{i}qa}$ and boundary continuity condition $U_{\mathrm{L}}\left(\frac{a}{2}\right) = U_{\mathrm{U}}\ \left(\frac{a}{2}\right)$, four equations about displacement can be determined as:

$$\begin{cases} A_1 = e^{-\mathrm{i}qa}\left[A_3 \cos\left(\dfrac{\omega}{c_{\mathrm{I}}} a\right) + A_4 \sin\left(\dfrac{\omega}{c_{\mathrm{I}}} a\right)\right] \\ A_5 = e^{-\mathrm{i}qa}\left[A_7 \cos\left(\dfrac{\omega}{c_{\mathrm{O}}} a\right) + A_8 \sin\left(\dfrac{\omega}{c_{\mathrm{O}}} a\right)\right] \end{cases}, \tag{3}$$

and

$$\begin{cases} A_1 \cos\left(\dfrac{\omega}{c_{\mathrm{I}}} \dfrac{a}{2}\right) + A_2 \sin\left(\dfrac{\omega}{c_{\mathrm{I}}} \dfrac{a}{2}\right) = A_3 \cos\left(\dfrac{\omega}{c_{\mathrm{I}}} \dfrac{a}{2}\right) + A_4 \sin\left(\dfrac{\omega}{c_{\mathrm{I}}} \dfrac{a}{2}\right) \\ A_5 \cos\left(\dfrac{\omega}{c_{\mathrm{O}}} \dfrac{a}{2}\right) + A_6 \sin\left(\dfrac{\omega}{c_{\mathrm{O}}} \dfrac{a}{2}\right) = A_7 \cos\left(\dfrac{\omega}{c_{\mathrm{O}}} \dfrac{a}{2}\right) + A_8 \sin\left(\dfrac{\omega}{c_{\mathrm{O}}} \dfrac{a}{2}\right) \end{cases}, \tag{4}$$

where q is the wave number of longitudinal waves propagating in the coupled meta-rod.

To solve the dispersion curve, four additional equations are required to formulate the eigenvalue equation. Besides the displacement continuity condition, stress continuity is one of the most widely used conditions in the eigenvalue analysis. For the case of a homogeneous bar $\sigma = ES\frac{\partial u}{\partial z}$, this leads to:

$$\begin{cases} \sigma_{\mathrm{I,L}} = -\rho_{\mathrm{I}} c_{\mathrm{I}} \omega A_1 \sin\left(\dfrac{\omega}{c_{\mathrm{I}}} z\right) + \rho_{\mathrm{I}} c_{\mathrm{I}} \omega A_2 \cos\left(\dfrac{\omega}{c_{\mathrm{I}}} z\right) \\ \sigma_{\mathrm{I,U}} = -\rho_{\mathrm{I}} c_{\mathrm{I}} \omega A_3 \sin\left(\dfrac{\omega}{c_{\mathrm{I}}} z\right) + \rho_{\mathrm{I}} c_{\mathrm{I}} \omega A_3 \cos\left(\dfrac{\omega}{c_{\mathrm{I}}} z\right) \end{cases}. \tag{5.a}$$

And similarly, for the outer pipe:

$$\begin{cases} \sigma_{\mathrm{O,L}} = -\rho_{\mathrm{O}} c_{\mathrm{O}} \omega A_5 \sin\left(\dfrac{\omega}{c_{\mathrm{O}}} z\right) + \rho_{\mathrm{O}} c_{\mathrm{O}} \omega A_6 \cos\left(\dfrac{\omega}{c_{\mathrm{O}}} z\right) \\ \sigma_{\mathrm{O,U}} = -\rho_{\mathrm{O}} c_{\mathrm{O}} \omega A_7 \sin\left(\dfrac{\omega}{c_{\mathrm{O}}} z\right) + \rho_{\mathrm{O}} c_{\mathrm{O}} \omega A_8 \cos\left(\dfrac{\omega}{c_{\mathrm{O}}} z\right) \end{cases}. \tag{5.b}$$

By applying the Bloch condition $\sigma(0) = \sigma(a)e^{-\mathrm{i}qa}$ to Eq. (5.a) and Eq. (5.b), we have:

$$\begin{cases} \rho_{\mathrm{I}} c_{\mathrm{I}} \omega A_2 = e^{-\mathrm{i}qa}\left[-\rho_{\mathrm{I}} c_{\mathrm{I}} \omega A_3 \sin\left(\dfrac{\omega}{c_{\mathrm{I}}} a\right) + \rho_{\mathrm{I}} c_{\mathrm{I}} \omega A_3 \cos\left(\dfrac{\omega}{c_{\mathrm{I}}} a\right)\right] \\ \rho_{\mathrm{O}} c_{\mathrm{O}} \omega A_6 = e^{-\mathrm{i}qa}\left[-\rho_{\mathrm{O}} c_{\mathrm{O}} \omega A_7 \sin\left(\dfrac{\omega}{c_{\mathrm{O}}} a\right) + \rho_{\mathrm{O}} c_{\mathrm{O}} \omega A_8 \cos\left(\dfrac{\omega}{c_{\mathrm{O}}} a\right)\right] \end{cases}. \tag{6}$$

The other two equations can be obtained by focusing on the stress equilibrium of the resonator. For the resonator, its governing equation can be written as:

$$Ma_{\mathrm{M}} + f_{\mathrm{M}} = 0, \tag{7}$$

where $a_{\mathrm{M}} = \mathrm{d}^2 u_{\mathrm{M}}/\mathrm{d}t^2$, a_{M} is the axial acceleration of a local resonator; u_{M} denotes the longitudinal displacement of local resonator, assumed that $u_{\mathrm{M}} = Be^{-\mathrm{i}\omega t}$; f_{M} denotes the interacting force between inner LR rod and NS system, which can be given by

$$f_{\mathrm{M}} = k_1\left(B - U_{\mathrm{I,L}}\left(\frac{a}{2}\right)\right) + k_2\left(B - U_{\mathrm{O,L}}\left(\frac{a}{2}\right)\right). \tag{8}$$

By substituting this expression into Eq. (7), the displacement within the whole structure can be coupled by:

$$B = \frac{k_1 U_{\mathrm{I,L}}\left(\frac{a}{2}\right) + k_2 U_{\mathrm{O,L}}\left(\frac{a}{2}\right)}{k_1 + k_2 - M\omega^2}, \tag{9}$$

where B is the longitudinal displacement amplitude of a local resonator. Since the stress are continues at $z = a/2$, we have $\sigma_{\mathrm{I,L}}\left(\frac{a}{2}\right) = \sigma_{\mathrm{I,U}}\left(\frac{a}{2}\right) + k_1\left[B - U_{\mathrm{I,L}}\left(\frac{a}{2}\right)\right]/S_{\mathrm{I}}$ and $\sigma_{\mathrm{O,L}}\left(\frac{a}{2}\right) = \sigma_{\mathrm{O,U}}\left(\frac{a}{2}\right) + k_1\left[B - U_{\mathrm{O,L}}\left(\frac{a}{2}\right)\right]/S_{\mathrm{O}}$. According to these stress continuity condition, two stress continuity equations can be written as:

$$
\begin{aligned}
&-\rho_I c_I \omega S_I A_1 \sin\left(\frac{\omega}{c_I}\frac{a}{2}\right)+\rho_I c_I \omega S_I A_2 \cos\left(\frac{\omega}{c_I}\frac{a}{2}\right)\\
&\quad=-\rho_I c_I \omega S_I A_3 \sin\left(\frac{\omega}{c_I}\frac{a}{2}\right)+\rho_I c_I \omega S_I A_4 \cos\left(\frac{\omega}{c_I}\frac{a}{2}\right)\\
&+\frac{k_1k_2}{k_1+k_2-M\omega^2}\left[A_5\cos\left(\frac{\omega}{c_O}\frac{a}{2}\right)+A_6\sin\left(\frac{\omega}{c_O}\frac{a}{2}\right)\right]\\
&\quad+\frac{(M\omega^2-k_2)k_1}{k_1+k_2-M\omega^2}\left[A_1\cos\left(\frac{\omega}{c_I}\frac{a}{2}\right)+A_2\sin\left(\frac{\omega}{c_I}\frac{a}{2}\right)\right],
\end{aligned}
\tag{10}
$$

and

$$
\begin{aligned}
&-\rho_O c_O \omega S_O A_5 \sin\left(\frac{\omega}{c_O}\frac{a}{2}\right)+\rho_O c_O \omega S_O A_6 \cos\left(\frac{\omega}{c_O}\frac{a}{2}\right)\\
&\quad=-\rho_O c_O \omega S_O A_7 \sin\left(\frac{\omega}{c_O}\frac{a}{2}\right)+\rho_O c_O \omega S_O A_8 \cos\left(\frac{\omega}{c_O}\frac{a}{2}\right)\Bigg]\\
&+\frac{k_1k_2}{k_1+k_2-M\omega^2}\left[A_1\cos\left(\frac{\omega}{c_I}\frac{a}{2}\right)+A_2\sin\left(\frac{\omega}{c_I}\frac{a}{2}\right)\right]\\
&+\left[\frac{(M\omega^2-k_1)k_2}{k_1+k_2-M\omega^2}-k_s\right]\left[A_5\cos\left(\frac{\omega}{c_O}\frac{a}{2}\right)+A_6\sin\left(\frac{\omega}{c_O}\frac{a}{2}\right)\right],
\end{aligned}
\tag{11}
$$

where S_I and S_O denote the cross-sectional area of the inner rod and outer pipe respectively.

$$U_O=P_3\cos\left(\frac{\omega}{c_O}z\right)+P_4\sin\left(\frac{\omega}{c_O}z\right). \tag{14.b}$$

Four equilibrium equations are required to solve the coupled dynamic response due to the introduction of four unknown status parameter P_1,P_2,P_3,P_4. By employed $\sigma = ES\frac{\partial u}{\partial z}$, the stress function of both inner rod and outer pipe can be written as:

$$\sigma_I=-\rho_I c_I \omega P_1\sin\left(\frac{\omega}{c_I}z\right)+\rho_I c_I \omega P_2\cos\left(\frac{\omega}{c_I}z\right), \tag{15.a}$$

$$\sigma_O=-\rho_O c_O \omega P_3\sin\left(\frac{\omega}{c_O}z\right)+\rho_O c_O \omega P_4\cos\left(\frac{\omega}{c_O}z\right). \tag{15.b}$$

According to the boundary continuity condition $U^j(0) = U^{j-1}(a)$, two equations relative to displacement can be given by

$$
\begin{cases}
P_1^j=P_1^{j-1}\cos\left(\frac{\omega}{c_I}a\right)+P_2^{j-1}\sin\left(\frac{\omega}{c_I}a\right)\\
P_3^j=P_3^{j-1}\cos\left(\frac{\omega}{c_O}a\right)+P_4^{j-1}\sin\left(\frac{\omega}{c_O}a\right)
\end{cases}. \tag{16}
$$

The internal force is described in Eq. (8). By substituting this force expression into Eq. (15), the stress at the adjacent unit cell junctions can be coupled as:

$$
\begin{cases}
\rho_I c_I \omega S_I P_2^j+\frac{k_1k_2}{k_1+k_2-M\omega^2}P_3^j+\frac{(M\omega^2-k_2)k_1}{k_1+k_2-M\omega^2}P_1^j=-\rho_I c_I \omega S_I P_1^{j-1}\sin\left(\frac{\omega}{c_I}a\right)+\rho_I c_I \omega S_I P_2^{j-1}\cos\left(\frac{\omega}{c_I}a\right)\\
\rho_O c_O \omega S_O P_4^j+\frac{k_1k_2}{k_1+k_2-M\omega^2}P_1^j+\left[\frac{(M\omega^2-k_1)k_2}{k_1+k_2-M\omega^2}-k_s\right]P_3^j=-\rho_O c_O \omega S_O P_3^{j-1}\sin\left(\frac{\omega}{c_O}a\right)+\rho_O c_O \omega S_O P_4^{j-1}\cos\left(\frac{\omega}{c_O}a\right)
\end{cases}. \tag{17}
$$

Concluding Eqs. ((3), (4), (6), (10) and (11) in a matrix form, we obtain

$$\mathbf{DA}=0, \tag{12}$$

where $\mathbf{A} = (A_1,A_2,A_3,A_4,A_5,A_6,A_7,A_8)^T$, and $\mathbf{D}$ is the matrix about status coefficients. To keep $\mathbf{D}$ with a non-trivial solution, we must have

$$\det(\mathbf{D})=0. \tag{13}$$

By solving Eq. (13), the dispersion relation of whole proposed structure can be obtained as an analytical basis for revealing its attenuation behaviour.

3.2. Derivation of wave transmittance

As analysed in Section 2, the mutual motions between the resonator and inner rod, as well as between the resonator and outer pipe, play important roles in the dynamic response of whole structure. To illustrate these motion characteristics and dynamic responses under the same excitation, wave transmittance of finite-length structures is further derived. Due to the specificity of continuity conditions adopted in TMM, the local coordinates of resonators are shifted to the adjacent unit cell junctions with the specific coordinates $z^j = 0, j = 1,2,\ldots N$. This change results in the integration of mode shape functions describing the left and right half parts, expressed as:

$$U_I=P_1\cos\left(\frac{\omega}{c_I}z\right)+P_2\sin\left(\frac{\omega}{c_I}z\right), \tag{14.a}$$

Define the state parameter vector $\mathbf{P}^j = \left(P_1^j,P_2^j,P_3^j,P_4^j\right)^T$, continuity conditions between unit cells can be derived as:

$$\mathbf{KP}^j=\mathbf{HP}^{j-1}, \tag{18}$$

where

$$
\mathbf{K}=\begin{bmatrix}
1 & 0 & 0 & 0\\
\dfrac{\frac{(M\omega^2-k_2)k_1}{k_1+k_2-M\omega^2}}{\rho_I c_I \omega S_I} & 1 & \dfrac{\frac{k_1k_2}{k_1+k_2-M\omega^2}}{\rho_I c_I \omega S_I} & 0\\
0 & 0 & 1 & 0\\
\dfrac{\frac{k_1k_2}{k_1+k_2-M\omega^2}}{\rho_O c_O \omega S_O} & 0 & \dfrac{\frac{(M\omega^2-k_1)k_2}{k_1+k_2-M\omega^2}-k_s}{\rho_O c_O \omega S_O} & 1
\end{bmatrix}, \tag{19.a}
$$

$$
\mathbf{H}=\begin{bmatrix}
\cos\left(\frac{\omega}{c_I}z\right) & \sin\left(\frac{\omega}{c_I}z\right) & 0 & 0\\
-\sin\left(\frac{\omega}{c_I}z\right) & \cos\left(\frac{\omega}{c_I}z\right) & 0 & 0\\
0 & 0 & \cos\left(\frac{\omega}{c_O}z\right) & \sin\left(\frac{\omega}{c_O}z\right)\\
0 & 0 & -\sin\left(\frac{\omega}{c_O}z\right) & \cos\left(\frac{\omega}{c_O}z\right)
\end{bmatrix}. \tag{19.b}
$$

Thus, after giving displacement incentives U^0 at the first unit cell, the transmittance from the first unit cell to the Nth unit cell can be identified by:

$$\begin{bmatrix} U_{\mathrm{I}}^{N} \\ 0 \\ U_{\mathrm{O}}^{N} \\ 0 \end{bmatrix} = \left(\mathbf{K}^{-1}\mathbf{H}\right)^{N} \begin{bmatrix} U_{\mathrm{I}}^{0} \\ \sigma_{\mathrm{I}}^{0} \\ U_{\mathrm{O}}^{0} \\ \sigma_{\mathrm{O}}^{0} \end{bmatrix}, \tag{20}$$

where U^N denote the output displacement transmitted to the last unit cell. Corresponding to the free boundary condition at the ends of both inner rod and outer pipe, the stress status of the Nth unit cell is naturally equal to zero. By solving Eq. (20), the transmissibility (TS) can be obtained by:

$$TS = 20\log_{10}\left(U^{N}/U^{0}\right). \tag{21}$$

Based on this expression, and combining Eq. (8), the displacement ratio (DR) occurred at the Nth unit cell between the resonator and inner rod, as well as the resonator and outer pipe, is given as follows:

$$DR = \begin{cases} \dfrac{U_{\mathrm{M}}^{N}}{U_{\mathrm{I}}^{N}} = \left[k_1 + k_2\left(\dfrac{U_{\mathrm{O}}^{N}}{U_{\mathrm{I}}^{N}}\right)\right] \Big/ \left(k_1 + k_2 - M\omega^2\right), \text{for the inner rod} \\ \dfrac{U_{\mathrm{M}}^{N}}{U_{\mathrm{O}}^{N}} = \left[k_1\left(\dfrac{U_{\mathrm{I}}^{N}}{U_{\mathrm{O}}^{N}}\right) + k_2\right] \Big/ \left(k_1 + k_2 - M\omega^2\right), \text{for the outer pipe} \end{cases} . \tag{22}$$

By these, we can simultaneously leverage both DR and TS to investigate how boundary stiffness and internal forces of the proposed coupled meta-rod govern their attenuation ability in different ranges.

4. Model validation

In this section, we perform validation studies as demonstrations and comparisons to the theoretical analysis derived in Section 3. For the dispersion relation, two validation cases are implemented: (i) setting $k_2 = k_1$ and $M = 0$, and (ii) setting $\rho_2 c_2 S_2 = k_2 = 0$. The phase coefficient, representing the band structure, is consequently computed in comparison with existing analysis frameworks. While for the transmissibility, we develop a three-dimensional (3D) finite element (FE) model to validate and further visualise the internal interaction within the proposed coupled meta-rod. This visualisation, demonstrated by wave field, provides a complementary analysis to investigate how the mutual motion influences the propagation characteristics in both application scenarios.

4.1. Unit cell model validation

Before starting our investigation on the attenuation mechanisms of the proposed coupled meta-rod, it is necessary to verify the availability and reliability of the present analytical model. The results of dispersion relation are compared with those of Chen and Elbanna (2017) and Lu et al. (2024) for the cases of the coupled bar and LR rod. Chen and Elbanna developed a solution for the coupled bar, in which springs act as flexible constraints connecting the two bars. Lu et al. stated a detailed solution for the LR rod based on the TMM, which has been validated by FE models. By removing the mass and setting the negative stiffness to positive in the present solution, the analytical model derived in Section 3.1 can be used to describe the above two scenarios. Keeping all material and geometric parameters consistent with those in references (Chen and Elbanna, 2017; Lu et al., 2024), the availability and reliability of the present analytical model are validated through these two degeneration studies.

Fig. 3 illustrates the dispersion relation of meta-rod in the absence of mass block and NS springs, respectively. The calculated results are marked by blue circles, and the existing results are represented by red squares. In the former case, only positive-stiffness springs are taken into account by setting $k_2 = k_1$ and $M = 0$ following those in Ref. (Lu et al., 2024). While in the second case, the term of k_2 and $\rho_2 c_2 S_2$ in the eigenvalue matrix are set to zero to simulate a typical LR rod without external constraints. A good agreement between the results can be observed, confirming that the phase coefficient indicated in dispersion relation curve can be properly and reliably captured by the proposed analytical model.

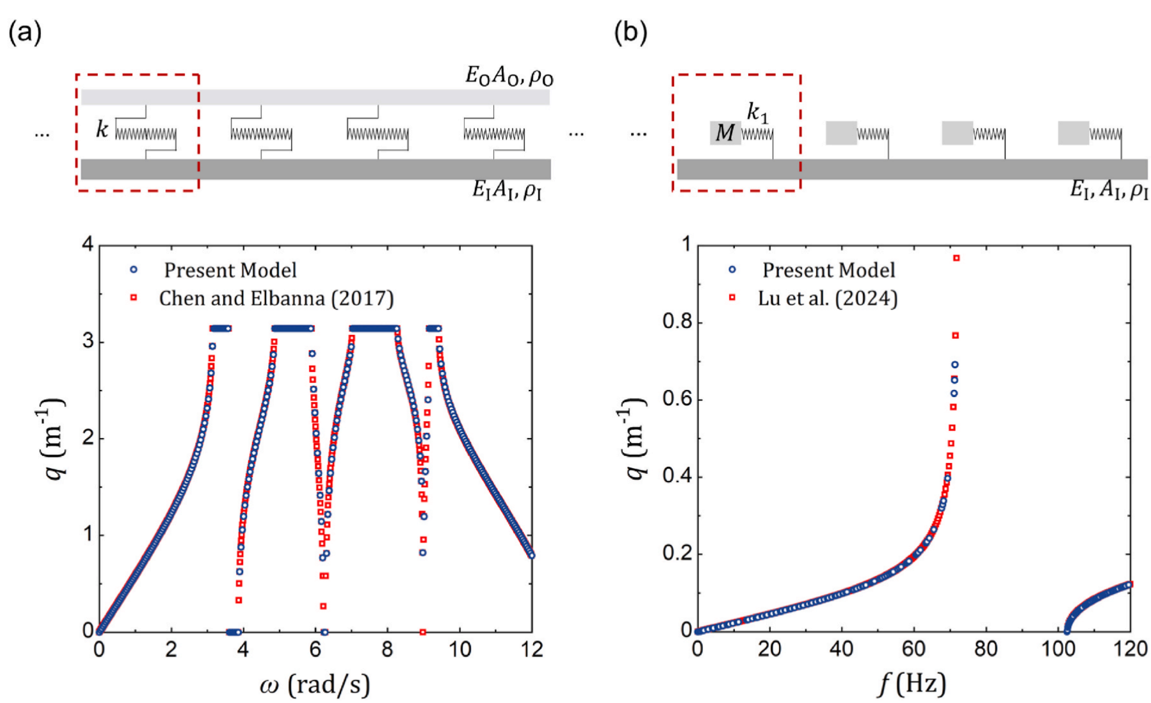

Fig. 3. Verification of the present model. (a) Dispersion relations when coupling of homogeneous bars by positive-stiffness springs; (b) Dispersion relations when using a homogeneous bar equipped with a resonator.

4.2. Transmission FE model validation

To verify the transmissibility of the proposed coupled meta-rod and further reveal the mutual motion in influencing the propagation characteristics, a 3D FE model is developed as a complement and comparison to the analytical results. In the context of the small-strain assumption, each component, including inner rod, rubber ring, metal ring, and outer pipe (see Fig. 2(a)), is modelled as a linear elastic material with Young's modulus, density, and Poisson's ratio in COMSOL Multiphysics. However, solid elements are employed to model the metal and rubber rings, which are simplified as a mass–spring system in the analytical model. The shear stiffness of rubber ring, namely k_1 in the analytical model, can be computed using the reference equation: $\frac{\pi r_r h E_r}{(1+\nu_r)t}$, where r_r is the radius of the inner rod; h, t are the height and thickness of rubber ring, respectively; the subscript "r" is used for the rubber material. The metal ring is also designed with specific geometrical dimensions to attain a mass corresponding to M in the analytical model.

Similar to the theoretical analysis, the coupled meta-rod is modelled by applying a free boundary on both sides and an imposed displacement on the bottom surface of the first unit cell. During the wave propagation, displacements occurred at the surface of jth resonator and jth outer pipe unit are monitored as the input to the computational expression of negative stiffness. Then, a couple of thrust forces generated by the NS spring are auto-applicated on the resonator and outer pipe within the jth unit cell, which can be calculated by

$$\begin{cases} F_{2,\mathrm{M}}^{j} = k_2\left(l\Big/\sqrt{b^2+\left(u_{\mathrm{M}}^{j}-u_{\mathrm{O}}^{j}\right)^2}-1\right)\left(u_{\mathrm{M}}^{j}-u_{\mathrm{O}}^{j}\right) \\ F_{2,\mathrm{O}}^{j} = k_2\left(l\Big/\sqrt{b^2+\left(u_{\mathrm{O}}^{j}-u_{M}^{j}\right)^2}-1\right)\left(u_{\mathrm{O}}^{j}-u_{\mathrm{M}}^{j}\right) \end{cases}, \tag{23}$$

where the subscripts "O" and "M" are used for the outer pipe and mass block, respectively; l is the original length of the compression spring; b is the deformed length of the compression spring at a static equilibrium state, with $b < l$. Moreover, the soil springs considered in the meta-pile application are also modelled in COMSOL by using Spring Foundation Module, with the spring constant given by k_s. The results computed by FE models are presented in Section 5 as a complement and comparison to the analytical results.

5. Results and discussion

In this section, we engage in a comparative analysis of the bandgap and attenuation ability of the proposed coupled meta-rod in the form of meta-column and meta-pile. By adjusting the geometric parameter, this coupled meta-rod is applied in two engineering scenarios: traffic-induced and seismic-induced vibration mitigation. We start by examining the bandgap properties to explain hybridised longitudinal wave modes propagating in different media. Subsequently, we validate and further explore how the internal interaction and boundary stiffness of meta-column and meta-pile govern their attenuation ability across different ranges, in comparison with FE-model results.

5.1. Application as meta-column for traffic-induced vibration mitigation

Rayleigh waves, known as a type of in-plane wave carrying most of the energy, are guided modes travelling at the free surface of an elastic half-space (Graff, 1991). These noteworthy energies generated by surface vibration sources propagate in the form of counterclockwise ellipse through the surrounding soil, subsequently influencing adjacent buildings. Compared to traffic-induced bulk waves, Rayleigh waves demonstrate distinct characteristics such as low attenuation rate and larger amplitudes, which are notably responsible for inducing structural vibrations (Ba et al., 2025). Especially for high-technology facilities, such as two-photon laser scanning microscopes and field emission scanning electron microscopy, Rayleigh wave-induced vibrations typically need to be controlled within an effective frequency band ranging of 0.5–100 Hz (Amick, 2005). Many researchers suggested building vertical resonators along the surface to inhibit the propagation of Rayleigh waves by locating them around the substrate (Palermo et al., 2016; Colombi et al., 2016). In this section, with the same objective of controlling the vertical Raleigh wave component, we perform more investigation on structure itself by detailing the characteristics of internal motions and interactions within the proposed meta-rod.

In engineering applications, large-diameter pillars are usually used to support protected devices against high-intensity vertical loads. Making reference to this solution, we introduce parameters that closely match the typical characteristics of columns in the structures adjacent to surface railways. The basic geometric and material parameters of the meta-column are listed in Table 1 to facilitate the following discussions. The material parameters of both inner rod and outer pipe are adopted as those of concrete, with reference to Lu et al. (2024). In addition to the equivalent parameter $k_1, k_1,$ and M used in theoretical analysis, the detailed geometric and material parameters employed in FE models are also listed in Table 1. Please note that the parameters are selected according to Table 1, except as specified in the figures.

5.1.1. Bandgap properties and wave attenuation behaviour of meta-column

First, let us start from the dispersion relation analysis of longitudinal waves interacting with meta-column units through the eigenvalue solution. By imposing the frequency $f \in [1, 150]$Hz and solving the eigenvalue problem (q, ω) described in Eq. (13), we plot the dispersion curve of longitudinal waves in meta-column installed on the surface of foundation, as shown in Fig. 4. The hybridized longitudinal wave mode is indicated by blue circles, with three specific eigenmodes at the branch edge highlighted by hexagram markers. For comparison, the pure longitudinal waves of the isolated inner rod and outer pipe are also plotted using red dash-dotted line as references in Fig. 4. Due to the coupling between longitudinal waves and the local resonator, it can be observed from the dispersion curve that the pure longitudinal wave mode is split as three hybridized branches: two around the resonance frequency f_r, one deviates from the original mode with a lower propagation speed. Generally, the region between the upper and lower bounds of the two branches separated by local resonance represents the LR bandgap. However, this phenomenon is not evident in the dispersion relation of meta-column due to the artificially imposed external constraint, which introduces additional modes between the split branches.

An amazing phenomenon can be observed in the first branch of the above dispersion relation curves: it starts with a larger wavenumber

Table 1
Geometric and material parameters details of the meta-column.

Specimen	Length	Exterior radius	Interior Radius	Young's modulus (E)	Density (ρ)	Poisson's ratio (υ)	Equivalent parameter (k or M)
Inner rod	0.25 m	0.45 m	–	40 Gpa	2500 $\mathrm{kg/m^3}$	0.3	–
Outer pipe	0.25 m	0.65 m	0.6 m				–
Rubber ring	0.204 m	0.454 m	0.45 m	3 Mpa	1300 $\mathrm{kg/m^3}$	0.47	1.47×10^8 N/m
Metal ring	0.232 m	0.575 m	0.454 m	200 Gpa	7890 $\mathrm{kg/m^3}$	0.3	716 Kg
Compression spring	0.15 m	–	–	–	–	–	-1.18×10^8 N/m

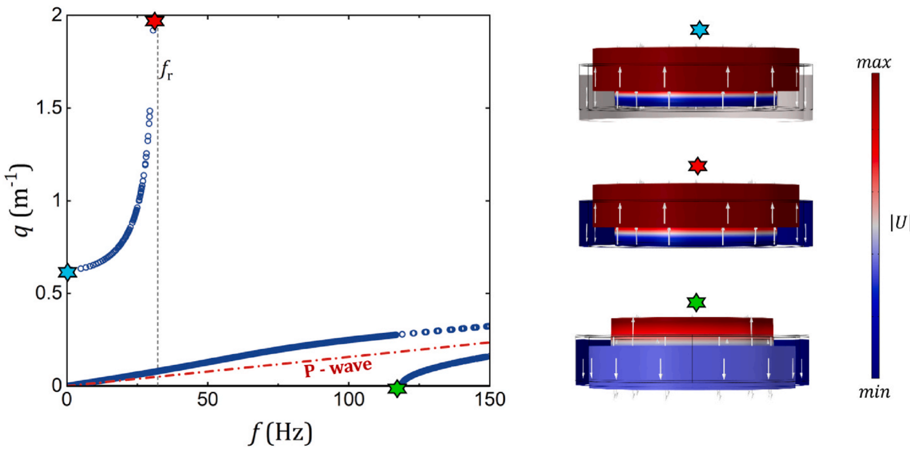

Fig. 4. Dispersion relation of longitudinal waves in meta-column installed on the surface of foundation. Three eigenmodes at the branch edge are labelled by hexagram. Blue circles denote the hybridised longitudinal wave mode, while red dash-dotted lines denote the pure longitudinal wave mode propagating in the inner rod and outer pipe. (For interpretation of the references to colour in this figure legend, the reader is referred to the Web version of this article.)

than that of typical LR dispersion relation curves. This indicates that a portion of longitudinal waves, especially near zero frequency, propagates in the meta-column with a lower speed and shorter wavelength. At this time, most of the energy concentrates in the transmission medium with lower rigidity, resulting in its redistribution between the inner rod and outer pipes. This phenomenon occurs in coupled meta-rod with stiffness contrast between longitudinal wave propagation media; however, it is absent in systems containing only a single propagation medium. We select characteristic locations at the edge of the first branch and the start of the third branch to illustrate vibration modes, which is plotted in the form of normalized displacement in the right panel of Fig. 4. As exhibited in the eigenmode labelled by cyan hexagram, it is evident that most of the wave energy concentrates in the outer pipe and resonator when connecting them via a NS spring. Then the motion is transmitted to the inner rod and resonator due to the local resonance of resonator. Eigenmodes labelled by red and green hexagrams also exhibit in-phase and out-of-phase motion between the inner rod and resonator, which are also identified as the bandgap edge in LR metamaterials analysis.

We then move to the dynamic response analysis of finite-length meta-column under an imposed displacement. Within a frequency range of interest $f \in [1, 60]$Hz, the transmissibility and displacement ratio of five-unit cells are computed and plotted in Fig. 5(a) and (b). The dynamic responses of the outer pipe and inner rod, as predicted by the analytical model and validated through FE simulations, are illustrated using red and blue lines for the theoretical results, and red and blue circles for the FE results, respectively. The first feature from Fig. 5(a) is that a significant drop occurs within transmissibility of outer pipe before a specific frequency f_1, while there is a response peak for the inner rod at this specific frequency. As the harmonic frequency increases, these two

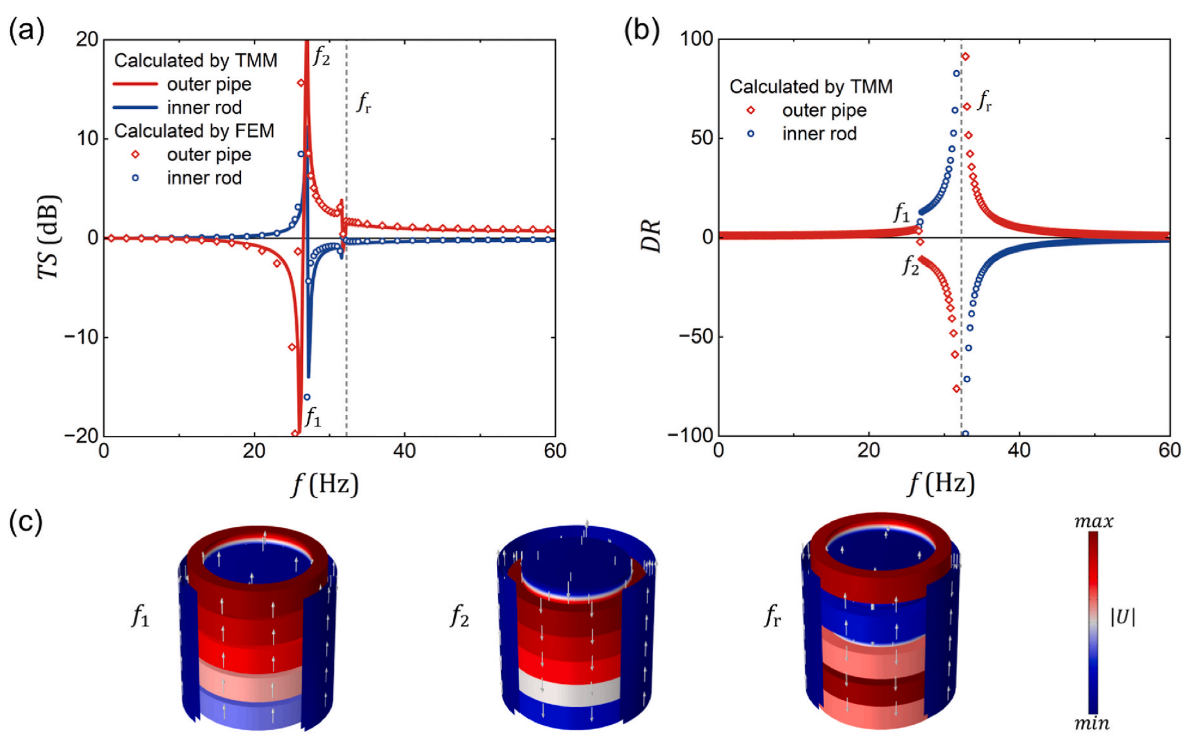

Fig. 5. Dynamic response curves of meta-column under an imposed displacement. (a) Transmissibility results calculated by two methods; (b) Displacement ratio curves for outer pipe and inner rod; (c) Displacement field occurred at $f = f_1, f_2, f_r$.

peaks subsequently reverse at another particular frequency f_2, yielding an attenuation of vertical vibration within the inner rod. It can also be observed from the transmissibility results that the response of inner rod bursts into a peak around f_r, which is exactly the natural frequency of the inside resonator. This widespread nature is generally found in the dynamic characteristics of LR metamaterials, which include the hybridisation modes of internal resonant with the wave propagation modes of the medium. Based on the above results, it can be concluded that the third peak originates from the resonance of inner resonator, while the first and second peaks may arise from the internal interaction within the meta-column.

To inspect mutual motions in the meta-column, we calculate the deformed shapes at f_1, f_2, f_r by using FE models, as shown in Fig. 5(c). Combining them with Fig. 5(b), the significant drop of outer pipe at f_1 is associated with the in-phase motion between three parts of meta-column, including outer pipe, resonator and inner rod. The displacement responses of outer pipe are suppressed by the resistance force F_2, which is generated by the NS spring. At this time, the inner rod, owing to its higher stiffness, steps ahead to attain the corresponding peaks. For the second peak at f_2, it is evident that the meta-column is precisely at a stage of transition where the motion between inner rod and resonator begins to reverse and that of outer pipe tends to be more intensive. At this point, due to the co-directional action of F_2, it turns into a part of contributions for the amplification effect of outer pipe responses. These mutual motions, resulting from the interactions within meta-column, provide different components with extra attenuation zones beyond bandgaps. As the frequency increases, the in-phase motion between the inner rod and resonator reach a peak at f_r, which corresponds to the local resonant mode discussed in Fig. 4. Due to the two different directions of motion occurring in five resonators, the attenuation ability of meta-column under this mechanism is weaker than that influenced by internal interaction analysed above.

5.1.2. Internal interaction effect within meta-column

Before starting our investigation on how the internal interaction governs their attenuation ability in different ranges, we define an index γ_k to describe the relation between the positive stiffness and negative stiffness, which can be given by $|k_2|/k_1$. This term, namely stiffness ratio, is usually used to indicate the stiffness counteracting degree occurred within the original resonant system. By tuning the stiffness or the compression length of compression springs, the internal force expressed in Eq. (8) is affected. As stated in the above analysis, the dynamic motions between the three parts of meta-column, including outer pipe, resonator and inner rod, are governed by this internal force.

Hence, our attention here is focused on the transmissibility variations under different stiffness ratios γ_k, as shown in Fig. 6. As γ_k increases, the response peaks of inner rod and outer pipe tend to separate from the resonance frequency $f_r(\gamma_k)$ highlighted by white dash line. This indicates that the main attenuation mechanism within the meta-column originates from its interaction with the longitudinal-wave propagation medium as the negative stiffness gradually converges to a positive stiffness value. Four representative curves beneath the contour plot further support this conclusion. The significant attenuation zone before f_r is tuned to the lower frequency range, while the attenuation zone at f_r tends to be weaker than the former. Based on this, the protected sensitive equipment can be put on the top surface of outer pipe to mitigate against the pounding of intense vertical vibration.

In engineering practices, the resonator can be installed with various distances and resonance frequencies along the length of meta-column. The inner rod, due to its inherent rigidity, can also be regarded as an artificial constraint to limit the motion of the outer pipe. To achieve more attenuation zones and enlarge their width, a symmetric placement strategy is adopted, in which half of the resonators are connected to the inner rod and the other half to the outer pipe, as illustrated in Fig. 7(a). This configuration is defined as condition A2. Furthermore, a gradient distribution of negative-stiffness (NS) springs is applied along the depth direction within each unit cell, with increasing stiffness values from top

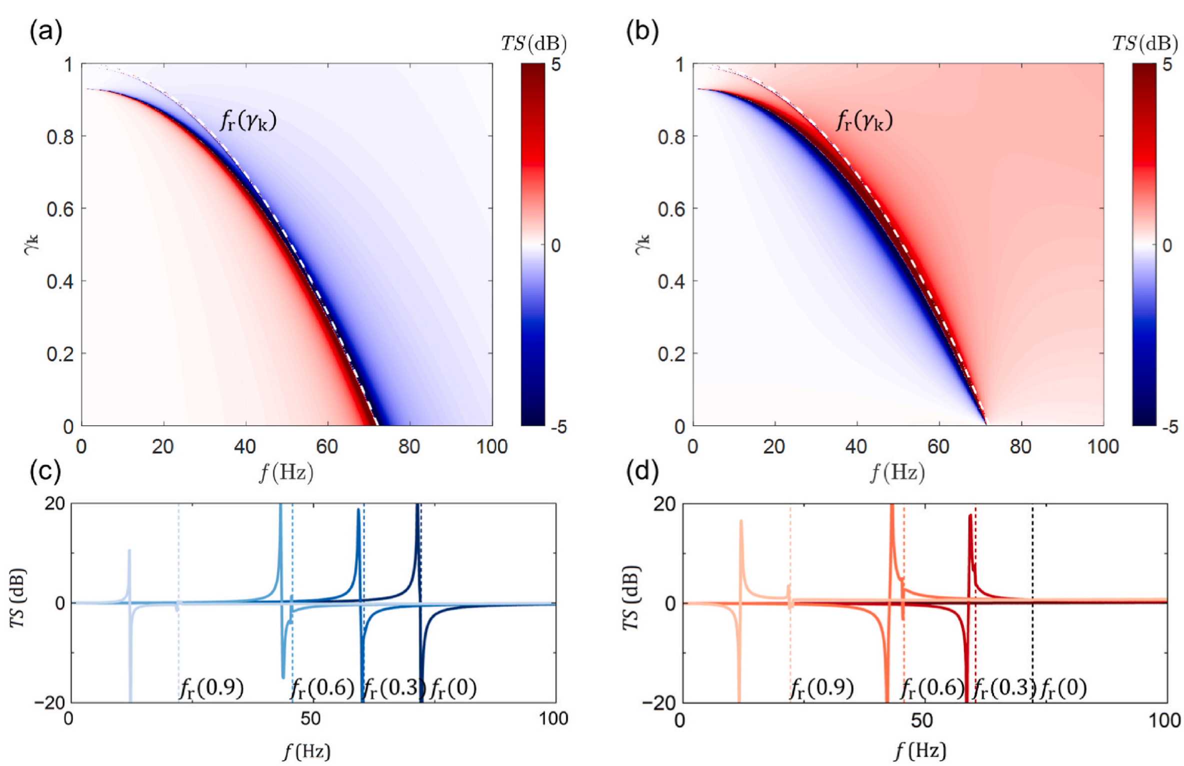

Fig. 6. Influence of the stiffness ratio on the transmissibility of (a) inner rod, and (b) outer pipe. Four representative curves of (c) inner rod, and (d) outer pipe are plotted under the contours figure when $\gamma_k = 0, 0.3, 0.6$, and 0.9.

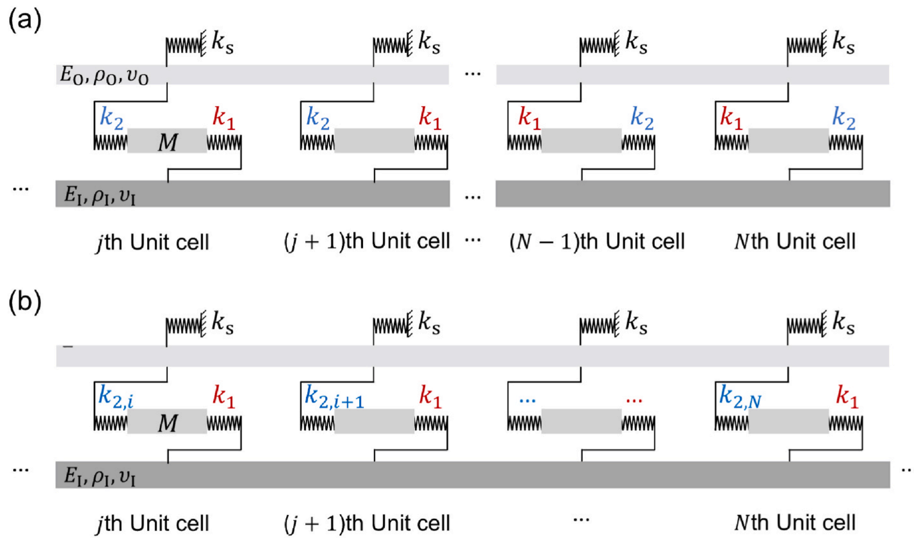

Fig. 7. Different connecting device placements: (a) A2: Symmetric distribution in the direction of depth; (b) A3: Gradient arrangement with a series of NS springs.

to bottom. This arrangement is defined as condition A3, as shown in Fig. 7(b). For comparison, the original configuration shown in Fig. 2(c) is referred to as condition A1. It should be noted that the soil spring plotted in Fig. 7 is automatically set to zero in the application scenario discussed in this section.

Fig. 8 illustrates transmissibility results and displacement ratio curves of six-unit cells under three placement conditions when subjected to an imposed displacement. The effect within the attenuation zone becomes effective in the A1 condition as the number of cells increases (see Fig. 8(a)), which is a well-established phenomenon. When adopting

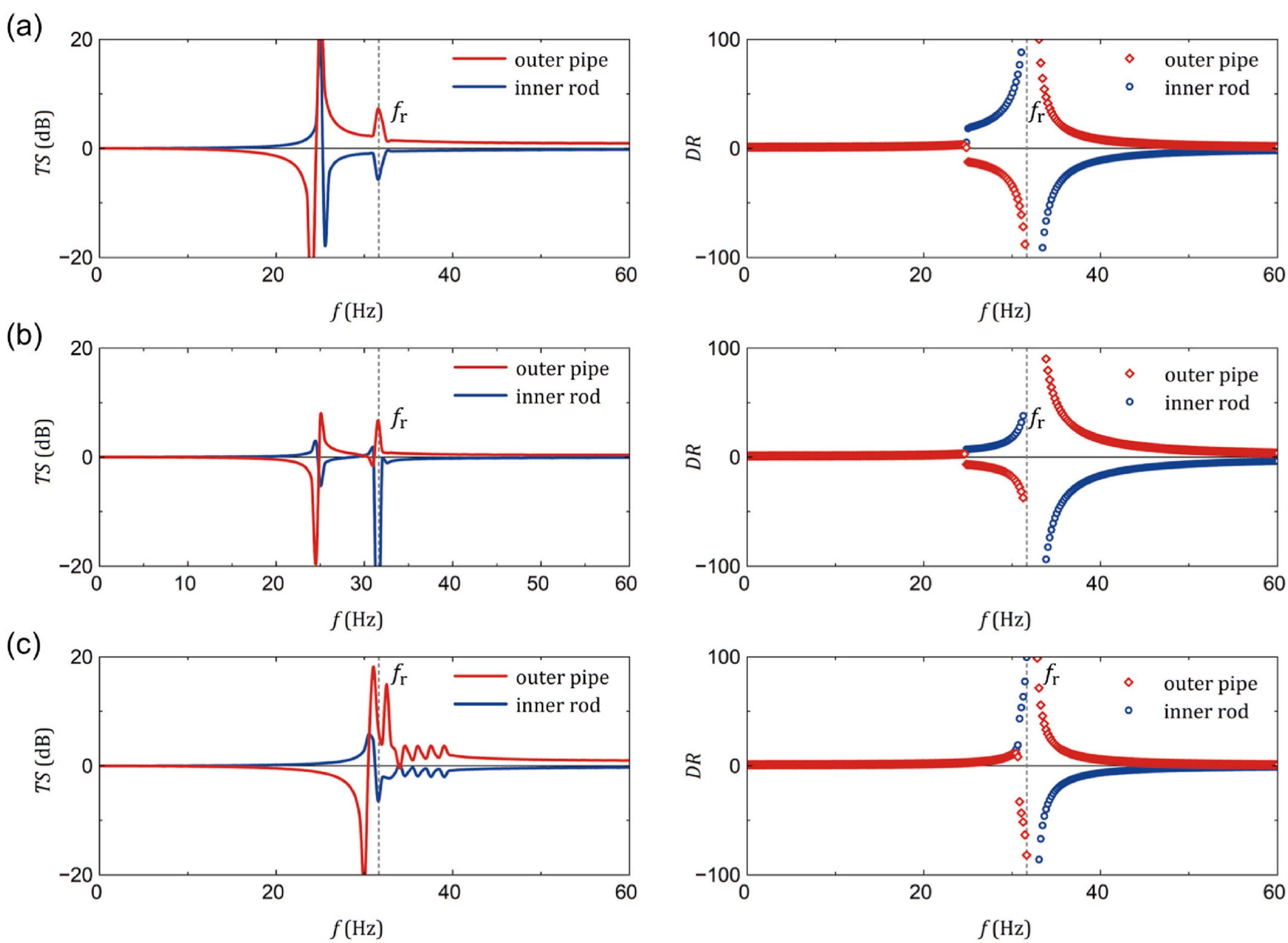

Fig. 8. Transmissibility results and displacement ratio curves of meta-column under an imposed displacement in (a) A1 condition; (b) A2 condition; (c) A3 condition.

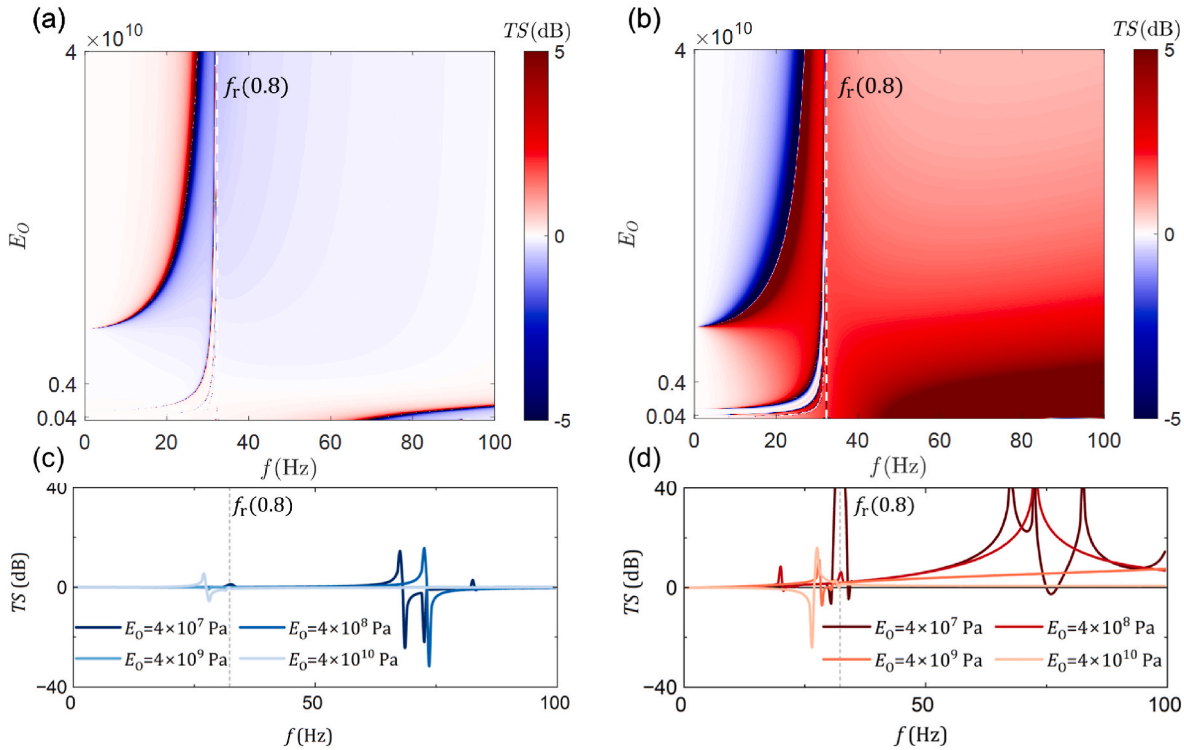

Fig. 9. The stiffness of outer pipe influences on the transmissibility of (a) inner rod, and (b) outer pipe under the A1 condition. A series of representative curves of (c) inner rod, and (d) outer pipe are plotted under the contours figure.

the symmetric distribution in the direction of depth, it is more distinct about the attenuation peak of inner rod at the resonance frequency. At this time, the motion of inner rod is more restricted than that in A1 condition, as shown in Fig. 8(b). The hybridisation of two connection forms induces the inner rod to open up a deeper attenuation zone when used as part of an artificial constraint. As the negative stiffness values are set within the range $\gamma_k \in [0.7, 0.8]$, a widened attenuation zone and more intense motion of inner rod and outer pipe are obtained around the resonance frequency, as shown in Fig. 8 (c). The attenuation peaks generated in different γ_k are merged to provide a stronger and wider effect.

5.1.3. Artificial constraints effect within meta-column

To elucidate the effect of artificial constraints on the attenuation mechanism of meta-column, the transmissibility of both inner rod and outer pipe are solved within $E_O \in [40\ \text{Kpa}, 40\ \text{Gpa}]$ and plotted in Fig. 9. It is evident that the NS system is barely functional when the modulus of the outer pile is lower. This phenomenon is represented in Fig. 9(a) as an original LR bandgap at the initial resonance frequency and is further demonstrated in Fig. 9(b) by a strong resonance response near this resonance frequency. As the modulus of the outer pile increases, this original bandgap is tuned to be near the reduced resonant frequency driven by negative stiffness. Interestingly, in addition to this modulation phenomenon, additional attenuation regions also emerge beyond the LR bandgap due to internal mutual motions. These regions become growingly effective and progressively shift toward the resonance frequency as the constraint increases.

5.2. Application as meta-pile for seismic-induced vibration mitigation

Now, we shift our focus to the mitigation of vibration induced by seismic waves. Compared to the vibration induced by traffic loads, seismic activities cause more severe dynamic responses transmitted from the piled foundation to the connected buildings. To shield target buildings from the vertical components of these dynamic responses, we embed the proposed coupled meta-rod in the ground and adjust its geometric parameters. Before investigating the characteristics of internal motions and interactions in this application scenario, we present some parameters that closely match the typical characteristics of piles in the structures.

The basic geometric and material parameters of the meta-pile are listed in Table 2. Besides the equivalent parameter k_1, k_1, and M used in theoretical analysis, the detailed geometric and material parameters of resonators employed in FE models are also listed in Table 2 to facilitate the following discussions. The surrounding soil, offering vertical resistance proportional to the motion of structures, is modelled with a series of springs in both analytical and numerical analyses. The stiffness value is calculated based on Winkler-Pasternak formulation:

Table 2
Geometric and material parameters details of the meta-pile.

Specimen	Length	Exterior radius	Interior Radius	Young's modulus (E)	Density (ρ)	Poisson's ratio (υ)	Equivalent parameter (k or M)
Inner rod	2 m	0.3 m	–	40 Gpa	2500 kg/m^3	0.3	–
Outer pipe	2 m	0.5 m	0.45 m	200 Gpa	7890 kg/m^3	0.3	–
Metal ring	0.856 m	0.36 m	0.31 m				711 Kg
Rubber ring	0.766 m	0.31 m	0.3 m	3 Mpa	1300 kg/m^3	0.47	1.47×10^8 N/m
Compression spring	0.15 m	–	–	–	–	–	-7.37×10^7 N/m

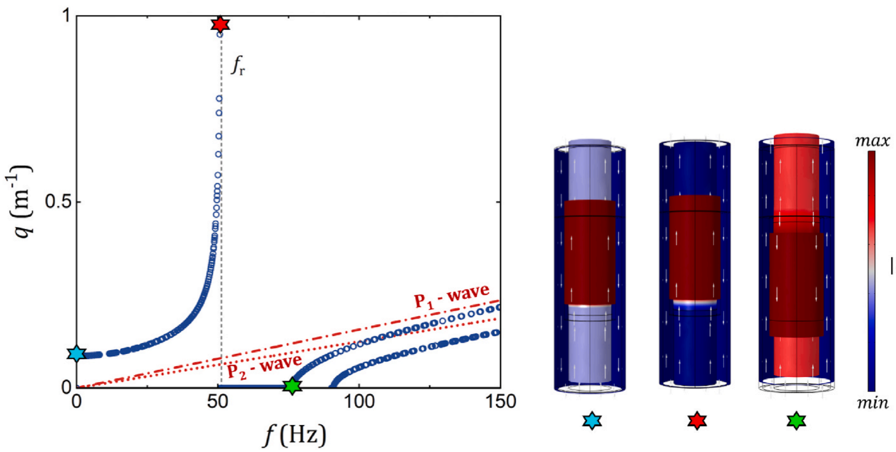

Fig. 10. Dispersion relation of longitudinal waves in meta-pile installed under the surface of foundation. Three eigenmodes at the branch edge are labelled by hexagram. Blue circles denote the hybridised longitudinal wave mode, while red dotted lines denote the two pure longitudinal wave modes propagating in the medium. (For interpretation of the references to colour in this figure legend, the reader is referred to the Web version of this article.)

$2\pi R_1\sqrt{C_1C_2}\,\frac{K_1\left(R_1\sqrt{C_1/C_2}\right)}{K_2\left(R_1\sqrt{C_1/C_2}\right)}$, where C_1, C_2 are the parameters characterizing the elastic foundation, and K_1, K_2 denote the modified Bessel functions. In this case, a stiff soil with a representative spring stiffness of $k_s = 7.85\times10^8$N/m is adopted as a reference condition for evaluating boundary constraints. The number of units varies depending on the specific working condition under consideration and is indicated in the relevant sections accordingly.

5.2.1. Bandgap properties and wave attenuation behaviour of meta-pile

By imposing the frequency of interest within $f\in[1,150]$Hz and solving the eigenvalue problem (q,ω) described in Eq. (13), we plot the dispersion curve of longitudinal waves in meta-pile installed in the foundation, as shown in Fig. 10. The pure longitudinal waves of the isolated inner rod and outer pipe, denoted as P_1- wave and P_2- wave, are also plotted using red dash-dotted line and dotted line, respectively. Obviously, the pure longitudinal wave mode is split into three hybridised branches due to the coupling between longitudinal waves and the local resonator, consistent with the analysis in section 5.1. The first and second branches are located around the frequency f_r, which is exactly the natural frequency f_r of the inside resonator. In these eigen solutions, two key features can be observed: (i) a portion of longitudinal waves propagates in the inner rod with a lower speed and shorter wavelength, especially near zero frequency; and (ii) the region between the upper and lower bounds of the first and second branches represent a distinct LR bandgap. These features are consistent with the stiffness of inner rod being less than that of the outer pipe under the constraints of soil spring. Most of the energy tends to concentrate on the inner rod at the low frequency, as illustrated by the blue hexagram symbol. This, in turn, leads to the hybridisation of the third branch associated with outer pipe occurring above the second branch.

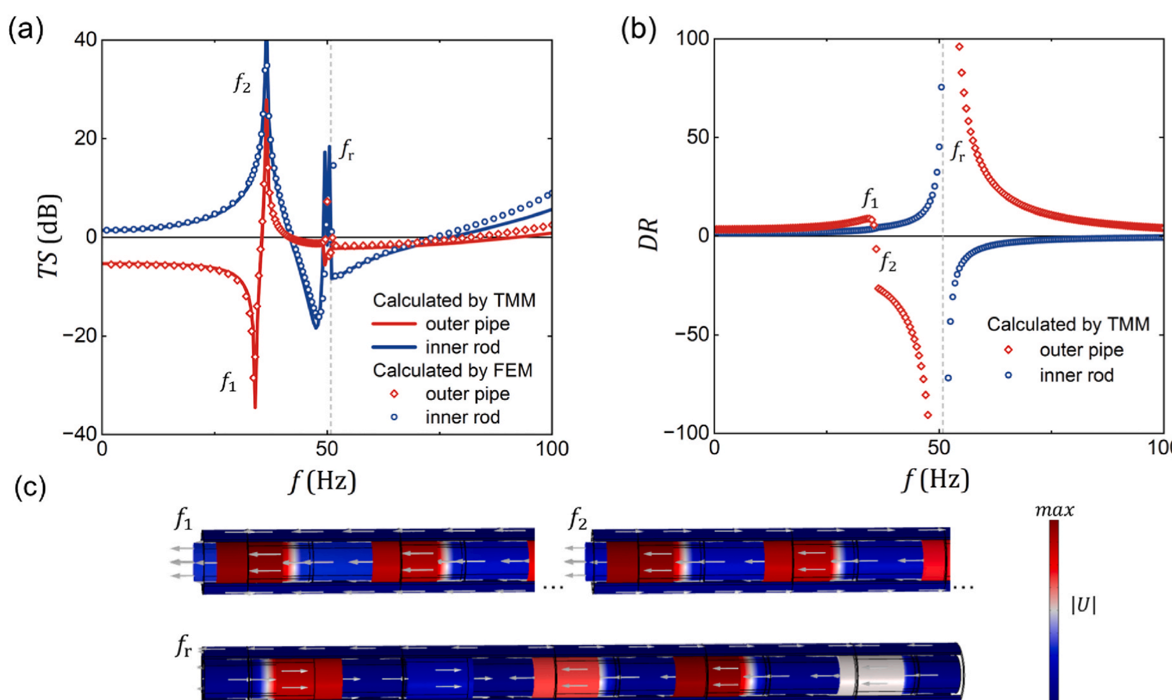

Fig. 11. Dynamic response curves of meta-pile under an imposed displacement. (a) Transmissibility results calculated by two methods; (b) Displacement ratio curves for outer pipe and inner rod; (c) Displacement field occurred at $f=f_1, f_2, f_r$.

To further validate and analyse the attenuation mechanism of meta-pile, the dynamic response curves of five-unit cells under an imposed displacement are presented in Fig. 11. The transmissibility results of inner rod and outer pipe, as computed by both theoretical model and FE models (see Fig. 11(a)), shows a distinct attenuation zone behind the resonance frequency f_r due to natural characteristics of the inside resonator. The deformed shapes at f_r (see Fig. 11(c)), also represent a typical resonant motion state, in which most of the wave energy is concentrated in internal resonators. However, additional effective attenuation zones are observed in meta-pile beyond this bandgap, particularly in the lower frequency range. Based on the analysis in Section 3.1, these attenuation zones originate from the in-phase motion and out-of-phase motion between inner rod, resonator, and outer pipe. The in-phase motion within meta-pile, as illustrated in Fig. 11(b) and (c), promotes the significant drop in the transmissibility curve of outer pipe at f_1. As the in-phase motion of outer pipe shifts to the motion with out-of-phase, the dynamic response of both inner rod and outer pipe reaches a peak at f_2. Then, the internal forces generated by positive- and negative-stiffness springs and external constraints originated from soil springs responsible for suppressing the dynamic response of inner rod and outer pipe, respectively. This phenomenon will persist until the internal resonator resonates. Moreover, the transmissibility curve of the inner rod exhibits noticeable attenuation near zero frequency, which results from the constraints imposed by the soil spring.

5.2.2. *Internal interaction effect within meta-pile*

We then move to investigate how the stiffness ratio influences the attenuation ability of meta-pile in different ranges. The results are plotted in Fig. 12 by tuning the stiffness of compression spring. For the inner rod, the first peak gradually moves towards and disappears in the lower frequency range as γ_k increases, while the second peak tends to separate from the resonance frequency $f_r(\gamma_k)$. The starting frequency of the LR bandgap is also gradually lowered, resulting in a wider bandgap but with reduced attenuation capability due to the increasingly dominant effect of F_2. However, it is evident that the significant attenuation zone before f_r, generated from the mutual motion within meta-pile, is progressively strengthened until γ_k is higher than about 0.8. The representative curves under the contour figure also illustrate this phenomenon. However, for the outer pipe, the attenuation zone appears at a frequency adjacent to the peaks of inner rod and is also shifted to the lower frequency range until it eventually disappears. These features indicate that the dynamic responses of both inner rod and outer pipe are suppressed from zero frequency as the internal force within meta-pile increases. Hence, this unit design can mitigate the adverse effect of deep sources acted on the target buildings, and the interaction between different propagation mediums can be exerted.

To further extend the width of attenuation zones, we also consider three placement conditions of springs and compute the transmissibility and displacement ratio of six-unit cells (see Fig. 13). The specific placements of both negative- and positive-stiffness springs can be found in Fig. 7. The difference here is about the A3 condition, where a gradation of negative stiffnesses with decreasing values is adopted along the direction of longitudinal wave propagation. Compared to the A1 condition, the A2 condition yields more effective attenuation zones across two distinct frequency ranges: the low-frequency range and the regions around the resonance frequency. This suggests that the combination of the symmetric distributions along the depth direction leads to the merging of attenuation peaks of the inner rod under both configurations, which aligns with the analysis presented in Section 5.1. For the A3 condition, we take values of NS within the range $\gamma_k \in [0.65, 0.5]$ to establish six resonance frequencies as shown in Fig. 13(c). The boundaries of these six LR bandgaps are coupled together, resulting in a wider combined bandgap without significant amplification peaks. This design provides a new approach to vibration isolation in different frequency ranges.

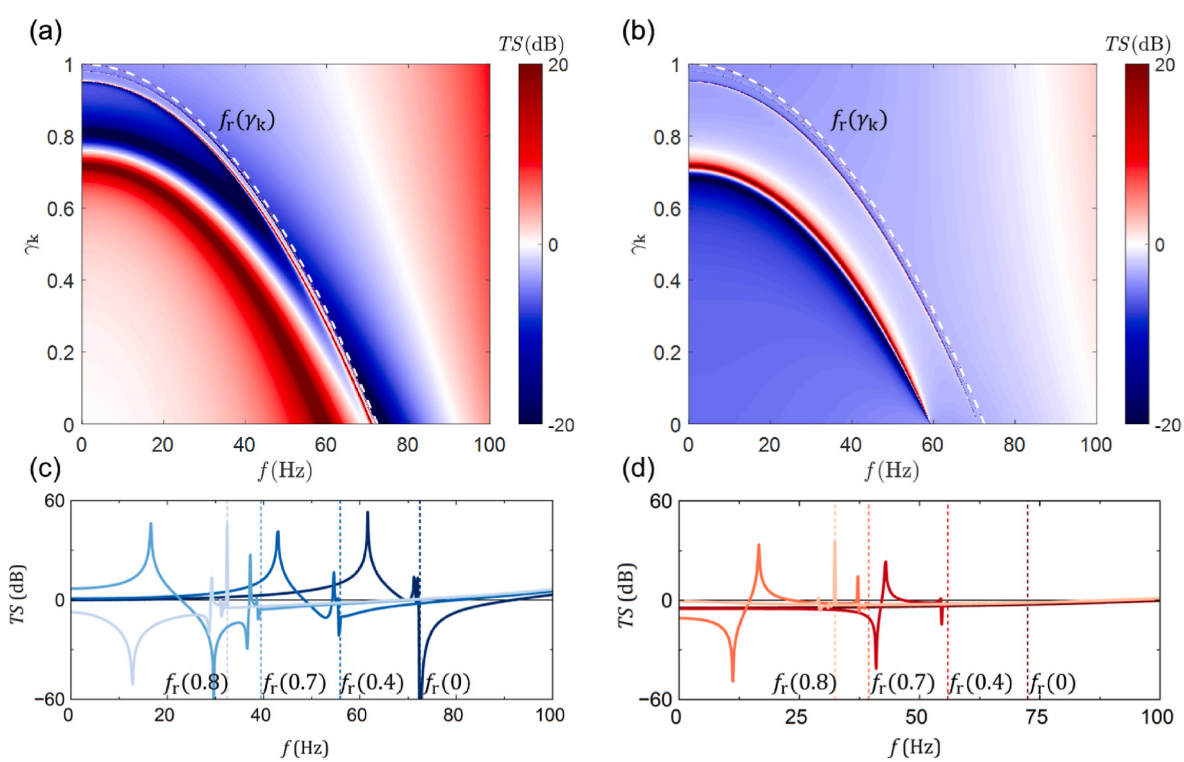

Fig. 12. Influence of the stiffness ratio on the transmissibility of (a) inner rod, and (b) outer pipe. Four representative curves of (c) inner rod, and (d) outer pipe are plotted under the contours figure as $\gamma_k = 0, 0.4, 0.7,$ and 0.8.

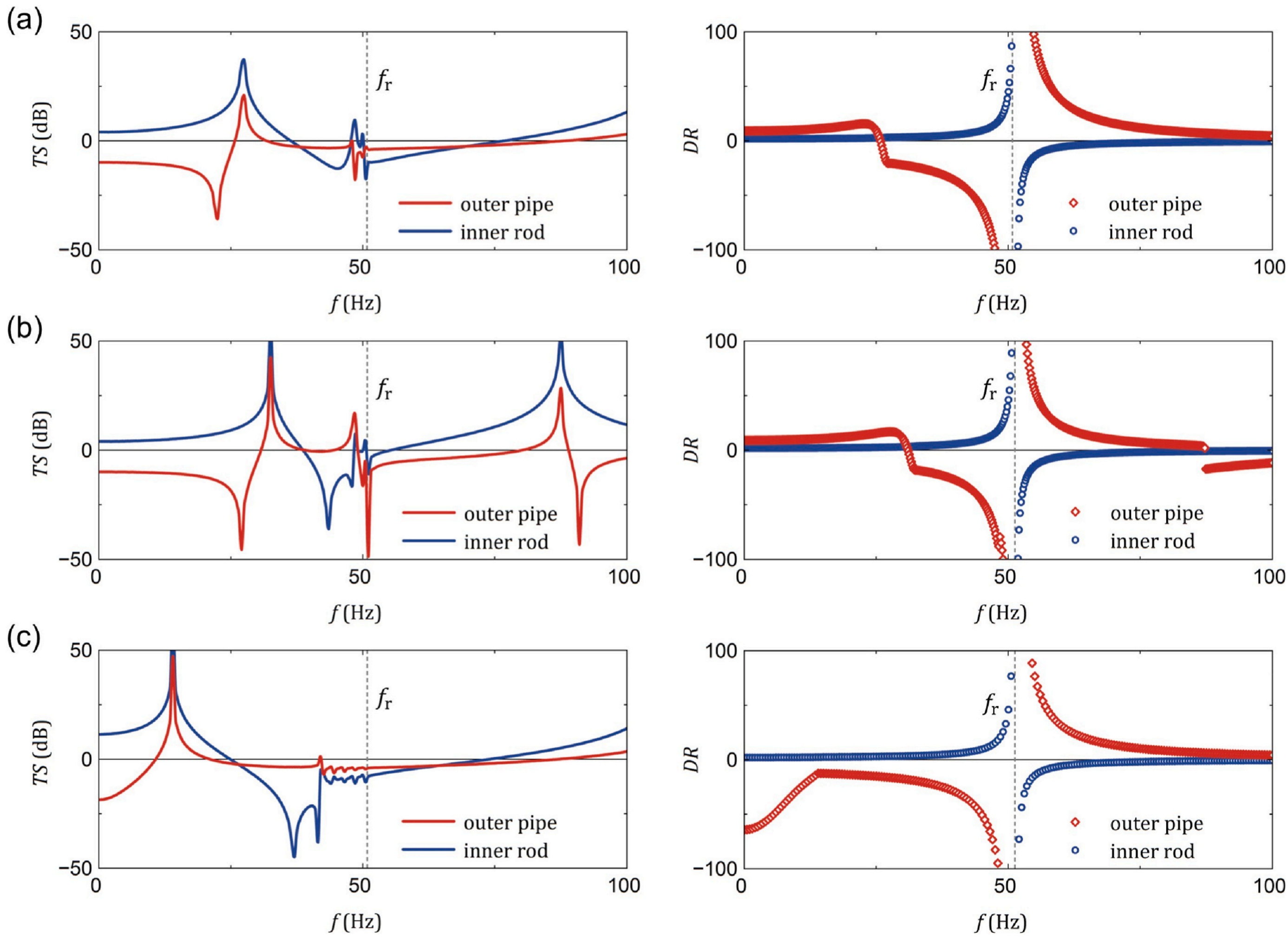

Fig. 13. Transmissibility results and displacement ratio curves of meta-pile under an imposed displacement in (a) A1condition; (b) A2 condition; (c) A3 condition.

5.2.3. *Boundary constraints effect within meta-pile*

In addition to the interaction within meta-pile, the boundary stiffness also plays an important role in attenuation mechanisms. Figs. 14 and 15 show the results of soil spring effect on the transmissibility of both inner and outer pipes under the original placement and inverse gradient placement, respectively. Obviously, the strength of the soil surrounding outer pile not only influences the width and intensity of its attenuation zone before the first response peak but also affects the attenuation zone of the inner rod by altering internal interactions. Fig. 14(c)–(d) and 15 (c)-(d) also indicate these trends in the frequency domain.

When adopting the A1 condition, the increase of k_s leads to a positive enhancement of the attenuation zone in both low-frequency range and regions after the resonance frequency, whereas this growth leads to a reduction in the attenuation effect before the resonance frequency. This phenomenon is totally changed under the A3 condition. As k_s increases, the broad attenuation zone of inner rod formed by the merging effect is more effective in the higher-frequency range. Meanwhile, the attenuation region of the outer pipe gradually shifts toward the lower-frequency range while maintaining an effective attenuation. Although stiffer soil provides a stronger restraining effect on the outer pipe, the A3 arrangement maintains effective suppression of vertical vibrations across different frequency regions, even in the presence of softer soil.

6. Discussions on the practical issues and options

In the above analysis, a pair of negative-stiffness springs are set in the gap between the inner rod and outer pipes. For practical engineering, it is necessary to install these springs that provide negative stiffness around the gap to maintain maximum force uniformity and structural stability. Besides compression springs employed in this work, devices capable of providing negative stiffness in certain forms can also be selected, such as coil springs (Wu and Lan, 2016), sliding block-bar springs (Wang et al., 2018), post-buckling beams (Cai et al., 2023), magnetic systems (Wang et al., 2020), and so on. Among them, springs and magnet systems are the most convenient for adjusting the internal thrust and then tuning the magnitude of negative stiffness, while post-buckling beams are the simplest way to implement the negative stiffness mechanism in practice. It is necessary to select a suitable negative stiffness facility depending on the application context.

This work proposed adjustment strategies for the stiffness ratio between negative and positive stiffness at different frequency ranges associated with isolation targets. In dense urban areas, where traffic loads dominate the vibration response, sensitive equipment operating in lower-frequency environments can be placed on the top of outer pipes with a larger stiffness ratio, whereas equipment functioning in higher-frequency environments can be installed on the top of inner rods

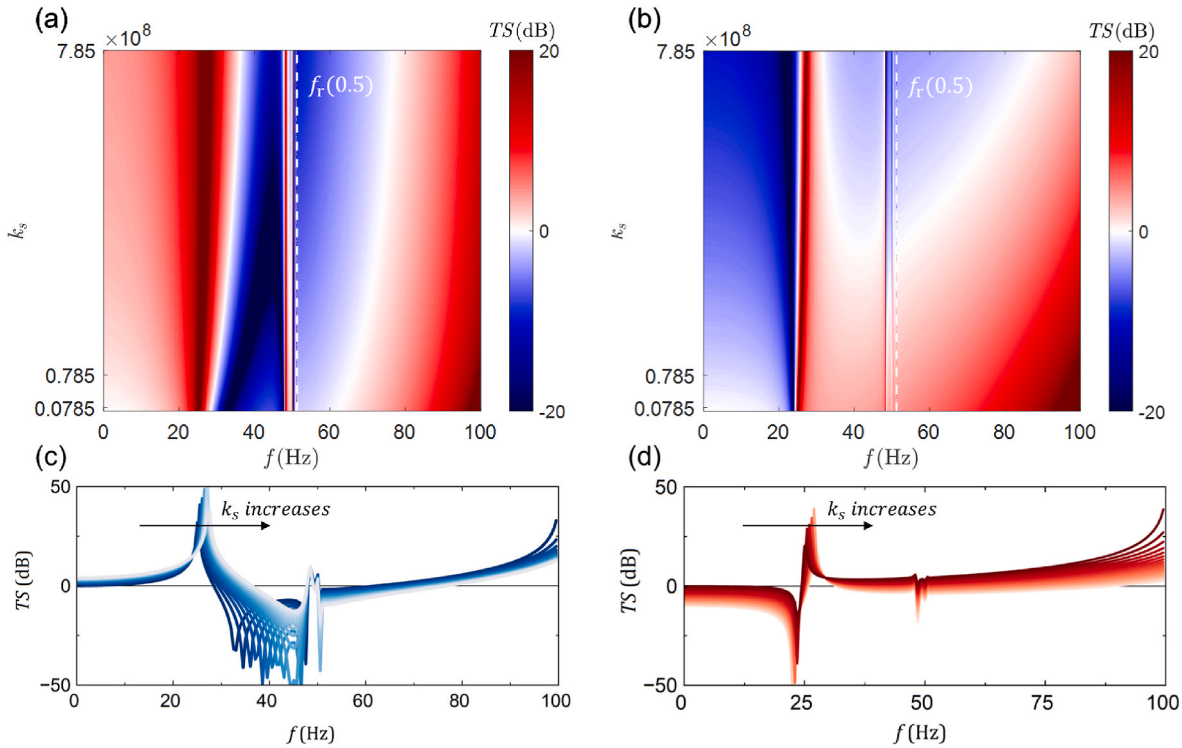

Fig. 14. The effects of soil spring stiffness on the transmissibility of (a) inner rod, and (b) outer pipe under A1 condition. A series of representative curves of (c) inner rod, and (d) outer pipe are plotted under the contours figure.

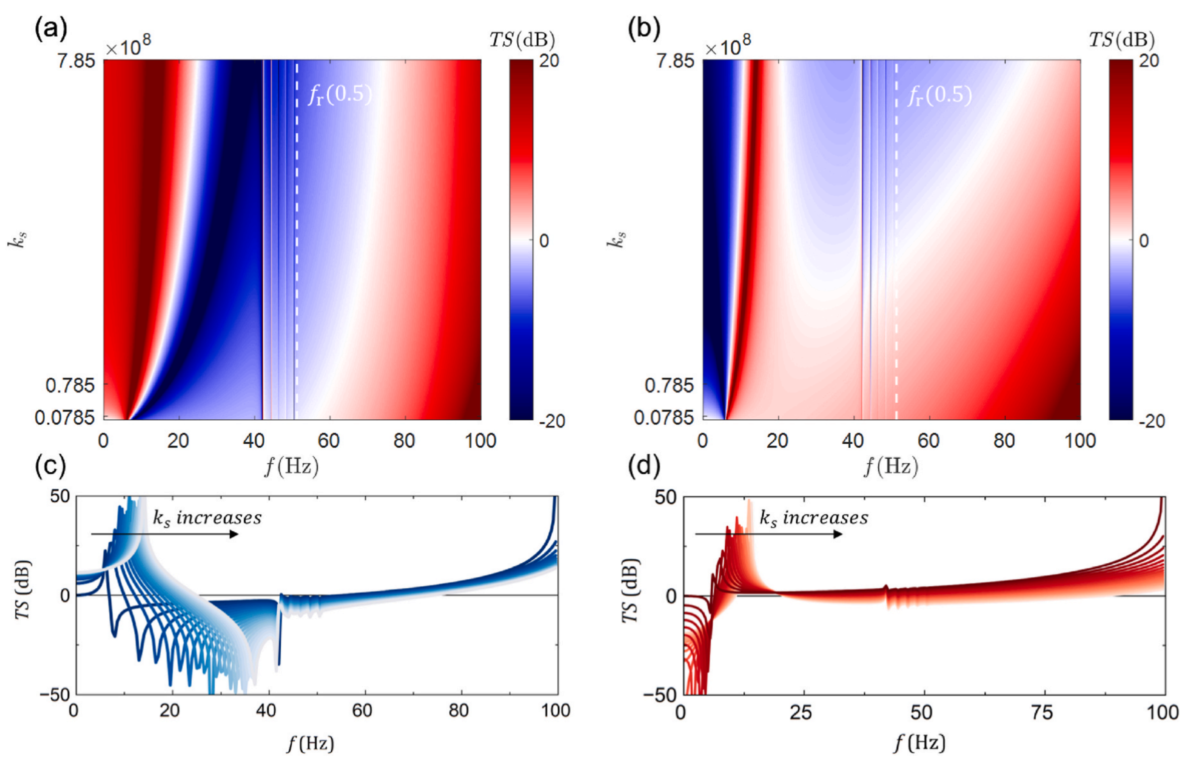

Fig. 15. The effects of soil spring stiffness on the transmissibility of (a) inner rod, and (b) outer pipe under A3 condition. A series of representative curves of (c) inner rod, and (d) outer pipe are plotted under the contours figure.

under A3 condition. Moreover, increasing the gradient magnitude and the number of graded units can further broaden the attenuation region, thereby facilitating the coverage of a wider target isolation frequency range. In seismic-impacted areas, the protecting structure can be constructed above the outer pipe with a lower negative stiffness when the surrounding soil is relatively rigid. However, if the soil barely provides external constraints, the inner rod or the outer pipe under A3 condition is the better choice.

7. Conclusions

In this study, we proposed a coupled meta-rod by utilising local resonance and negative stiffness mechanism, aiming to control and mitigate the in-plane polarised bulk waves and vertical Raleigh wave component generated by environmental vibrations. The analytical analyses are performed to elucidate the internal interaction and boundary stiffness effect of the coupled meta-rod and to understand their attenuation mechanisms comprehensively. The eigenmodes by FEM, as a complement and comparison to the analytical results, also validate the redistribute of wave energy within coupled meta-rod. The main findings are summarised as follows.

1. The pure longitudinal wave mode is split into three hybridised branches: two around the resonance frequency, and one deviates from the original longitudinal wave mode. Most of the energy concentrates on the transmission medium with lower rigidity, holding a lower speed and shorter wavelength, especially near zero frequency.
2. The in-phase motion between the three components of the coupled meta-rod promotes significant drops in transmissibility curves of the outer pipe before the LR bandgap. As the motion of the outer pipe transitions from in-phase to out-of-phase, these two dips in the transmission curves are subsequently transformed into peaks, accompanied by an attenuation region within the inner rod. This effect arises from internal forces created by positive and negative-stiffness springs, which provide direction-dependent amplification or suppression effects on dynamic response.
3. The negative stiffness system exhibits effective performance when the artificial boundary constraints possess relatively high stiffness. The primary attenuation mechanism of the coupled meta-rod arises from the internal interaction between distinct longitudinal-wave propagation media when the value of negative stiffness gradually converges to the positive stiffness. More low-frequency and effective attenuation regions are obtained by tuning the stiffness ratio between negative and positive stiffness according to isolation targets.

CRediT authorship contribution statement

Haoran Lu: Writing – review & editing, Writing – original draft, Software, Methodology, Investigation, Conceptualization. **Jacopo M. De Ponti:** Writing – review & editing, Methodology, Investigation. **Raffaele Ardito:** Writing – review & editing, Methodology. **Li Xiao:** Writing – review & editing, Software. **Yuanqiang Cai:** Supervision, Funding acquisition. **Zhigang Cao:** Writing – review & editing, Supervision, Funding acquisition.

Declaration of competing interest

The authors declare that they have no known competing financial interests or personal relationships that could have appeared to influence the work reported in this paper.

Acknowledgements

The work was supported by the National Natural Science Foundation of China (Grant No. 51978611), Natural Science Foundation for Outstanding Scholar in Zhejiang Province (Grant No. LR21E080004), and Center for Balance Architecture of Zhejiang University. H.R. Lu greatly acknowledges the support by Zhejiang University.

Data availability

Data will be made available on request.

References

Achaoui, Y., Antonakakis, T., Brûlé, S., Craster, R.V., Enoch, S., Guenneau, S., 2017. Clamped seismic metamaterials: ultra-low frequency stop bands. New J. Phys. 19, 063022. https://doi.org/10.1088/1367-2630/aa6e21.
Ali, S.F., Ramaswamy, A., 2009. Hybrid structural control using magnetorheological dampers for base isolated structures. Smart Mater. Struct. 18, 055011. https://doi.org/10.1088/0964-1726/18/5/055011.
Amick, H., 2005. On generic vibration criteria for advanced technology facilities: with a tutorial on vibration data representation. Journal of the IES 40, 35–44. https://doi.org/10.17764/jiet.2.40.5.f113t722560181j4.
Ba, Z., Yu, F., Kuo, C., Liu, Z., Liang, J., 2025. Seismic evaluation of arbitrary number of buildings resting on a layered half-space under incident rayleigh waves. Eng. Anal. Bound. Elem. 175, 106226. https://doi.org/10.1016/j.enganabound.2025.106226.
Barkan, D.D., 1962. Dynamics of Bases and Foundations. McGraw-Hill, New York.
Brûlé, S., Javelaud, E.H., Enoch, S., Guenneau, S., 2014. Experiments on seismic metamaterials: molding surface waves. Phys. Rev. Lett. 112, 133901. https://doi.org/10.1103/PhysRevLett.112.133901.
Cabello, M., Zurbitu, J., Renart, J., Turon, A., Martínez, F., 2016. A general analytical model based on elastic foundation beam theory for adhesively bonded DCB joints either with flexible or rigid adhesives. Int. J. Solid Struct. 94–95, 21–34. https://doi.org/10.1016/j.ijsolstr.2016.05.011.
Cai, C., Zhou, J., Wu, L., Wang, K., Xu, D., Ouyang, H., 2020. Design and numerical validation of quasi-zero-stiffness metamaterials for very low-frequency band gaps. Compos. Struct. 236, 111862. https://doi.org/10.1016/j.compstruct.2020.111862.
Cai, C., Zhou, J., Wang, K., Lin, Q., Xu, D., Wen, G., 2023. Quasi-zero-stiffness metamaterial pipe for low-frequency wave attenuation. Eng. Struct. 279, 115580. https://doi.org/10.1016/j.engstruct.2022.115580.
Cao, Z., Cai, Y., 2013. Isolation of train-induced ground-borne vibration by trenches on a poroelastic half-space. J. Eng. Mech. 139, 580–593. https://doi.org/10.1061/(ASCE)EM.1943-7889.0000460.
Carrella, A., Brennan, M.J., Waters, T.P., Lopes, V., 2012. Force and displacement transmissibility of a nonlinear isolator with high-static-low-dynamic-stiffness. Int. J. Mech. Sci. 55, 22–29. https://doi.org/10.1016/j.ijmecsci.2011.11.012.
Chang, C.-M., Shia, S., Lai, Y.-A., 2018. Seismic design of passive tuned mass damper parameters using active control algorithm. J. Sound Vib. 426, 150–165. https://doi.org/10.1016/j.jsv.2018.04.017.
Chen, Q., Elbanna, A., 2017. Emergent wave phenomena in coupled elastic bars: from extreme attenuation to realization of elastodynamic switches. Sci. Rep. 7, 16204. https://doi.org/10.1038/s41598-017-16364-8.
Christopoulos, C., Filiatrault, A., 2022. Principles of Passive Supplemental Damping and Seismic Isolation, second ed. second ed. Pavia: Eucentre.
Clouteau, D., Degrande, G., Lombaert, G., 2001. Numerical modelling of traffic induced vibrations. Meccanica 36, 401–420. https://doi.org/10.1023/A:1015005410628.
Colombi, A., Colquitt, D., Roux, P., Guenneau, S., Craster, R.V., 2016. A seismic metamaterial: the resonant metawedge. Sci. Rep. 6, 27717. https://doi.org/10.1038/srep27717.
Colquitt, D.J., Colombi, A., Craster, R.V., Roux, P., Guenneau, S.R.L., 2017. Seismic metasurfaces: sub-Wavelength resonators and rayleigh wave interaction. J. Mech. Phys. Solid. 99, 379–393. https://doi.org/10.1016/j.jmps.2016.12.004.
Dalela, S., Balaji, P.S., Jena, D.P., 2022. A review on application of mechanical metamaterials for vibration control. Mech. Adv. Mater. Struct. 29, 3237–3262. https://doi.org/10.1080/15376494.2021.1892244.
DeBra, D.B., 1992. Vibration isolation of precision machine tools and instruments. CIRP Annals 41, 711–718. https://doi.org/10.1016/S0007-8506(07)63257-0.
Demir, M.U., Yilmaz, C., 2022. Analysis and design of an adjustable stiffness three-axis horizontal vibration isolator using elastic columns and a string in tension. J. Sound Vib. 523, 116736. https://doi.org/10.1016/j.jsv.2021.116736.
Fang, X., Hao, H., Bi, K., 2021. Passive vibration control of engineering structures based on an innovative column-in-column (CIC) concept. Eng. Struct. 242, 112599. https://doi.org/10.1016/j.engstruct.2021.112599.
Fang, X., Hao, H., Bi, K., Song, J., Cao, Y., Chen, Z., 2024. Optimization of column-in-column system based on non-conventional TMD concept. Int. J. Mech. Sci. 279, 109497. https://doi.org/10.1016/j.ijmecsci.2024.109497.
Feng, M.Q., Mita, A., 1995. Vibration control of tall buildings using mega SubConfiguration. J. Eng. Mech. 121, 1082–1088. https://doi.org/10.1061/(ASCE)0733-9399(1995)121:10(1082.
Gao, G.Y., Li, Z.Y., Qiu, Ch, Yue, Z.Q., 2006. Three-dimensional analysis of rows of piles as passive barriers for ground vibration isolation. Soil Dynam. Earthq. Eng. 26, 1015–1027. https://doi.org/10.1016/j.soildyn.2006.02.005.
Graff, K.F., 1991. Wave Motion in Elastic Solids. Dover Publications, New York.
Griefahn, B., Marks, A., Robens, S., 2006. Noise emitted from road, rail and air traffic and their effects on sleep. J. Sound Vib. 295, 129–140. https://doi.org/10.1016/j.jsv.2005.12.052.
Han, Y., Chen, X., Wei, Y., Jiang, S., Du, C., Jiang, G., et al., 2025. Vibration attenuation of metamaterial dual-beam with simultaneous acoustic Black hole and local resonator. Eur. J. Mech. Solid. 111, 105535. https://doi.org/10.1016/j.euromechsol.2024.105535.
Huang, X., Liu, X., Sun, J., Zhang, Z., Hua, H., 2014. Vibration isolation characteristics of a nonlinear isolator using euler buckled beam as negative stiffness corrector: a theoretical and experimental study. J. Sound Vib. 333, 1132–1148. https://doi.org/10.1016/j.jsv.2013.10.026.
Jiang, S., Bi, K., Ma, R., Xu, K., 2024. $H\infty$ closed-form solution of tuned mass damper enhanced with negative stiffness element (TMD-NS) for structural vibration control. J. Sound Vib. 586, 118510. https://doi.org/10.1016/j.jsv.2024.118510.

Jiao, P., Mueller, J., Raney, J.R., Zheng, X., Rayne, Alavi, A.H., 2023. Mechanical metamaterials and beyond. Nat. Commun. 14, 6004. https://doi.org/10.1038/s41467-023-41679-8.
Kanellopoulos, C., Psycharis, N., Yang, H., Jeremić, B., Anastasopoulos, I., Stojadinović, B., 2022. Seismic resonant metamaterials for the protection of an elastic-plastic SDOF system against vertically propagating seismic shear waves (SH) in nonlinear soil. Soil Dynam. Earthq. Eng. 162, 107366. https://doi.org/10.1016/j.soildyn.2022.107366.
Kochmann, D.M., Milton, G.W., 2014. Rigorous bounds on the effective moduli of composites and inhomogeneous bodies with negative-stiffness phases. J. Mech. Phys. Solid. 71, 46–63. https://doi.org/10.1016/j.jmps.2014.06.010.
Kuo, K.A., Papadopoulos, M., Lombaert, G., Degrande, G., 2019. The coupling loss of a building subject to railway induced vibrations: numerical modelling and experimental measurements. J. Sound Vib. 442, 459–481. https://doi.org/10.1016/j.jsv.2018.10.048.
Lakes, R.S., 2001. Extreme damping in composite materials with a negative stiffness phase. Phys. Rev. Lett. 86, 2897–2900. https://doi.org/10.1103/PhysRevLett.86.2897.
Lakes, R.S., Lee, T., Bersie, A., Wang, Y.C., 2001. Extreme damping in composite materials with negative-stiffness inclusions. Nature 410, 565–567. https://doi.org/10.1038/35069035.
Lin, S., Zhang, Y., Liang, Y., Liu, Y., Liu, C., Yang, Z., 2021. Bandgap characteristics and wave attenuation of metamaterials based on negative-stiffness dynamic vibration absorbers. J. Sound Vib. 502, 116088. https://doi.org/10.1016/j.jsv.2021.116088.
Liu, Z., Zhang, X., Mao, Y., Zhu, Y.Y., Yang, Z., Chan, C.T., et al., 2000. Locally resonant sonic materials. Science 289, 1734–1736. https://doi.org/10.1126/science.289.5485.1734.
Liu, Y., Shen, X., Su, X., Sun, C.T., 2016. Elastic metamaterials with low-frequency passbands based on lattice system with On-Site potential. J. Vib. Acoust. 138. https://doi.org/10.1115/1.4032326.
Lu, H., Cao, Z., Xiao, L., Cai, Y., Xu, Y., 2024. A new meta-rod attenuating low-frequency waves with external fixed supporting. Int. J. Mech. Sci. 264, 108832. https://doi.org/10.1016/j.ijmecsci.2023.108832.
Maheshwari, H.K., Rajagopal, P., 2022. [Fixed in a concrete slab]Novel locally resonant and widely scalable seismic metamaterials for broadband mitigation of disturbances in the very low frequency range of 0–33 Hz. Soil Dynam. Earthq. Eng. 161, 107409. https://doi.org/10.1016/j.soildyn.2022.107409.
Makris, N., Gazetas, G., 1992. Dynamic pile-soil-pile interaction. Part II: lateral and seismic response. Earthq. Eng. Struct. Dynam. 21, 145–162. https://doi.org/10.1002/eqe.4290210204.
Mei, C., Li, L., Jiang, Y., Ye, Y., Li, X., Han, X., et al., 2023. On band gap and damping of metamaterials involving negative-stiffness elements. Int. J. Mech. Sci. 239, 107877. https://doi.org/10.1016/j.ijmecsci.2022.107877.
Palermo, A., Krödel, S., Marzani, A., Daraio, C., 2016. Engineered metabarrier as shield from seismic surface waves. Sci. Rep. 6, 39356. https://doi.org/10.1038/srep39356.
Ramaswamy, N., Joshi, B., Wang, J., Li, X., Menq, F.Y., Shan, X., et al., 2023. Experimental study of passive seismic vibration isolation by trench-type periodic barrier. Eng. Struct. 276, 115308. https://doi.org/10.1016/j.engstruct.2022.115308.
Rodrigues, C., Simões, F.M.F., Pinto da Costa, A., Froio, D., Rizzi, E., 2018. Finite element dynamic analysis of beams on nonlinear elastic foundations under a moving oscillator. Eur. J. Mech. Solid. 68, 9–24. https://doi.org/10.1016/j.euromechsol.2017.10.005.
Segol, G., Abel, J.F., Lee, P.C.Y., 1978. Amplitude reduction of surface waves by trenches. J. Eng. Mech. Div. 104, 621–641. https://doi.org/10.1061/JMCEA3.0002365.
Setareh, M., 2001. Application of semi-active tuned mass dampers to base-excited systems. Earthq. Eng. Struct. Dynam. 30, 449–462. https://doi.org/10.1002/eqe.19.
Song, Y., Panas, R.M., Chizari, S., Shaw, L.A., Jackson, J.A., Hopkins, J.B., et al., 2019. Additively manufacturable micro-mechanical logic gates. Nat. Commun. 10, 882. https://doi.org/10.1038/s41467-019-08678-0.
Sugino, C., Ruzzene, M., Erturk, A., 2018. Merging mechanical and electromechanical bandgaps in locally resonant metamaterials and metastructures. J. Mech. Phys. Solid. 116, 323–333. https://doi.org/10.1016/j.jmps.2018.04.005.
Tan, X., Wang, L., Zhu, S., Chen, S., Wang, B., Kadic, M., 2022. A general strategy for performance enhancement of negative stiffness mechanical metamaterials. Eur. J. Mech. Solid. 96, 104702. https://doi.org/10.1016/j.euromechsol.2022.104702.
Tan, X., Zhu, S., Wang, B., Kadic, M., 2024a. Tuning negative stiffness mechanical metamaterial's snap-through behavior with a series-connected spring. Eur. J. Mech. Solid. 107, 105382. https://doi.org/10.1016/j.euromechsol.2024.105382.
Tan, X., Cao, B., Liu, X., Zhu, S., Chen, S., Kadic, M., et al., 2024b. Negative stiffness mechanical metamaterials: a review. Smart Mater. Struct. 34, 013001. https://doi.org/10.1088/1361-665x/ad97fe.
Thompson, D.J., Jiang, J., Toward, M.G.R., Hussein, M.F.M., Ntotsios, E., Dijckmans, A., et al., 2016. Reducing railway-induced ground-borne vibration by using open trenches and soft-filled barriers. Soil Dynam. Earthq. Eng. 88, 45–59. https://doi.org/10.1016/j.soildyn.2016.05.009.
Thompson, D.J., Kouroussis, Georges, Ntotsios, E., 2019. Modelling, simulation and evaluation of ground vibration caused by rail vehicles. Veh. Syst. Dyn. 57, 936–983. https://doi.org/10.1080/00423114.2019.1602274.
Tuan, A.Y., Shang, G.Q., 2014. Vibration control in a 101-Storey building using a tuned mass damper. Journal of Applied Science and Engineering 17, 141–156. https://doi.org/10.6180/jase.2014.17.2.05.
Vo, N.H., Pham, T.M., Bi, K., Chen, W., Hao, H., 2021. Stress wave mitigation properties of dual-meta panels against blast loads. Int. J. Impact Eng. 154, 103877. https://doi.org/10.1016/j.ijimpeng.2021.103877.
Vo, N.H., Pham, T.M., Hao, H., Bi, K., Chen, W., 2022. A reinvestigation of the spring-mass model for metamaterial bandgap prediction. Int. J. Mech. Sci. 221, 107219. https://doi.org/10.1016/j.ijmecsci.2022.107219.
Wang, X., Liu, H., Chen, Y., Gao, P., 2018. Beneficial stiffness design of a high-static-low-dynamic-stiffness vibration isolator based on static and dynamic analysis. Int. J. Mech. Sci. 142–143, 235–244. https://doi.org/10.1016/j.ijmecsci.2018.04.053.
Wang, K., Zhou, J., Ouyang, H., Cheng, L., Xu, D., 2020. A semi-active metamaterial beam with electromagnetic quasi-zero-stiffness resonators for ultralow-frequency band gap tuning. Int. J. Mech. Sci. 176, 105548. https://doi.org/10.1016/j.ijmecsci.2020.105548.
Wang, K., Zhou, J., Cai, C., Xu, D., Xia, S., Wen, G., 2021. Bidirectional deep-subwavelength band gap induced by negative stiffness. J. Sound Vib. 515, 116474. https://doi.org/10.1016/j.jsv.2021.116474.
Wang, X., Wan, S., Zhou, P., Fu, J., Wu, Z., 2023. Vibration mitigation in porous soil using periodic rock-socketed pile barriers. Soil Dynam. Earthq. Eng. 171, 107956. https://doi.org/10.1016/j.soildyn.2023.107956.
Wang, Y., Wang, K.F., Wang, B.L., 2025. Torsional bandgap characteristics in metamaterial rods with multiple internal multi-degree-of-freedom resonators. Eur. J. Mech. Solid. 112, 105663. https://doi.org/10.1016/j.euromechsol.2025.105663.
Woods, R.D., 1968. Screening of surface wave in soils. J. Soil Mech. Found Div. 94, 951–979. https://doi.org/10.1061/JSFEAQ.0001180.
Woods, R.D., Barnett, N.E., Sagesser, R., 1974. Holography—A new tool for soil dynamics. J. Geotech. Eng. Div. 100, 1231–1247. https://doi.org/10.1061/AJGEB6.0000121.
Wu, T.-H., Lan, C.-C., 2016. A wide-range variable stiffness mechanism for semi-active vibration systems. J. Sound Vib. 363, 18–32. https://doi.org/10.1016/j.jsv.2015.10.024.
Xiao, L., Iqbal, M., Yu, X., 2024. Quasi-static band gaps in metamaterial pipes with negative stiffness resonators. Int. J. Mech. Sci. 261, 108668. https://doi.org/10.1016/j.ijmecsci.2023.108668.
Xu, Y., Cao, Z., Yuan, Z., Cai, Y., Alves Costa, P., 2023. Analytical research on the mitigation of structure-borne vibrations from subways using locally resonant periodic foundations. J. Eng. Mech. 149, 04022083. https://doi.org/10.1061/(ASCE)EM.1943-7889.0002160.
Yang, Y.-B., Hung, H.-H., 1997. A parametric study of wave barriers for reduction of train-induced vibrations. Int. J. Numer. Methods Eng. 40, 3729–3747. https://doi.org/10.1002/(SICI)1097-0207(19971030)40:20<3729::AID-NME236>3.0.CO;2-3747.
Yu, P., Zhang, Y., Gao, Z., Song, W., Zhao, Y., 2020. Structural microvibration monitoring and simulation analysis of the proton service building based on the construction process. Structures 27, 1841–1850. https://doi.org/10.1016/j.istruc.2020.07.075.
Zemskov, A.V., Van Hao, L., 2025. Unsteady thermoelastic-diffusive vibrations of a bernoulli-euler beam on an elastic foundation. Eur. J. Mech. Solid. 113, 105707. https://doi.org/10.1016/j.euromechsol.2025.105707.
Zhang, Z., Li, X., Zhang, X., Xu, G., Wu, A., 2024. Measurements and evaluation of road traffic-induced micro-vibration in a workshop equipped with precision instruments. Buildings 14, 1142. https://doi.org/10.3390/buildings14041142.
Zheng, H., Han, S., Li, S., Han, Q., Li, C., 2024. A novel multi-resonator honeycomb metamaterial with enhanced impact mitigation. Eur. J. Mech. Solid. 105, 105272. https://doi.org/10.1016/j.euromechsol.2024.105272.
Zhou, J., Wang, K., Xu, D., Ouyang, H., 2017. Local resonator with high-static-low-dynamic stiffness for lowering band gaps of flexural wave in beams. J. Appl. Phys. 121, 044902–044902.
Zhou, W., Li, Y., Yan, G., Zhou, J., 2024. Quasi-full bandgap generating mechanism by coupling negative stiffness and inertial amplification. Eur. J. Mech. Solid. 103, 105143. https://doi.org/10.1016/j.euromechsol.2023.105143.